

Energy evolution and leading logarithm- $1/x$ approximation in QCD

We now begin the presentation of our main subject: high energy QCD, also known as small- x physics. We argue that at small Bjorken x it is natural to try to resum leading logarithms of $1/x$, that is, powers of $\alpha_s \ln 1/x$. Resummation of this parameter in the linear approximation corresponding to low parton density is accomplished by the Balitsky–Fadin–Kuraev–Lipatov (BFKL) evolution equation, which we describe in this chapter using the standard approach based on Feynman diagrams. Note that our derivation of the BFKL equation in this chapter is rather introductory in nature; a more rigorous re-derivation employing LCPT is left until for the next chapter. We point out some problems with the linear BFKL evolution; in particular we argue that it violates unitarity constraints for the scattering cross section. We describe initial attempts to solve the BFKL unitarity problem by introducing nonlinear corrections to the BFKL evolution, resulting in the Gribov–Levin–Ryskin and Mueller–Qiu (GLR–MQ) evolution equation. We discuss properties of the GLR–MQ evolution equation and, for the first time, introduce the saturation scale Q_s .

3.1 Paradigm shift

Our goal in this book is to study the high energy behavior of QCD. In the context of DIS the high energy asymptotics can be explored by fixing the photon virtuality Q^2 and taking the photon–proton center-of-mass energy squared \hat{s} to be large. In this limit the Bjorken- x variable becomes small, as follows from Eq. (2.6). The small- x asymptotics is therefore synonymous with the high energy limit of QCD:

$$\text{small } x \iff \text{high energy } s. \quad (3.1)$$

The small- x asymptotics of the gluon distribution function $xG(x, Q^2)$ in the framework of DGLAP evolution was discussed in Section 2.4.6. For the LLA DGLAP, the small- x asymptotics corresponds to summation of the parameter

$$\alpha_s \ln \frac{1}{x} \ln \frac{Q^2}{Q_0^2}, \quad (3.2)$$

which constitutes the double logarithm approximation (DLA). While in Sec. 2.4.6 we worked out the running coupling case, the small- x asymptotics of the gluon distribution function for fixed coupling can be shown to be that in Eq. (2.159). The resulting gluon

Table 3.1. *The transverse and longitudinal leading logarithmic approximations (LLAs) and the double logarithmic approximation (DLA)*

Approximation	Coupling	Transverse logarithm	Longitudinal logarithm
LLA in Q^2	$\alpha_s(Q^2) \ll 1$	$\alpha_s \ln(Q^2/Q_0^2) \approx 1$	$\alpha_s \ln 1/x \ll 1$
LLA in $1/x$	$\alpha_s \ll 1$	$\alpha_s \ln(Q^2/Q_0^2) \ll 1$	$\alpha_s \ln 1/x \approx 1$
DLA	$\alpha_s(Q^2) \ll 1$	$\alpha_s \ln(Q^2/Q_0^2) \ll 1$ $\alpha_s \ln 1/x \ll 1$ but $\alpha_s \ln(Q^2/Q_0^2) \ln 1/x \approx 1$	

distribution grows with decreasing x in such a way that

$$\left(\frac{1}{x}\right)^a \gg xG(x, Q^2) \propto \exp\left(2\sqrt{\frac{\alpha_s N_c}{\pi} \ln \frac{1}{x} \ln \frac{Q^2}{Q_0^2}}\right) \gg \ln^n \frac{1}{x}, \tag{3.3}$$

which is faster than any positive power n of $\ln 1/x$ but slower than any positive power a of $1/x$.

The asymptotics of the gluon distribution (3.3) is valid in the double logarithmic limit of small x and large Q^2 . However, if one is interested in studying the high energy (Regge) limit of QCD, one simply needs to fix Q^2 at some, not necessarily large, value and study the small- x asymptotics. As there is no need to take the large- Q^2 limit, $\ln(Q^2/Q_0^2)$ is now neither a large nor a small parameter. We therefore drop it from Eq. (3.2) and aim to resum the parameter

$$\alpha_s \ln \frac{1}{x}. \tag{3.4}$$

Resummation of a series in powers of the parameter (3.4) is referred to as the leading-logarithmic approximation (LLA) in $1/x$. As with previous logarithmic approximations we assume that the relevant transverse momentum scales are large enough that $\alpha_s \ll 1$. At small x we have $\ln 1/x \gg 1$, so that $\alpha_s \ln 1/x \sim 1$ and is an important parameter to resum. (Indeed, as we have seen from Sec. 2.4.6 already, and as will be clear from the calculations below, for gluon distribution functions and for total hadronic scattering cross sections one can have at most one power of $\ln 1/x$ per power of the coupling α_s , i.e., there is no resummation parameter like $\alpha_s \ln^2 1/x$ in xG though there are other observables, such as $\Delta^{f\bar{f}}$, which depend on this parameter: however, these are suppressed at high energy and the presentation of their low- x asymptotics is beyond the scope of this book.) As we will see in the next chapter, the resummation of gluon emissions in the light cone wave function presented in Sec. 2.4.2 can also be done in the LLA in $1/x$ instead of the LLA in Q^2 , as used for DGLAP evolution.

Table 3.1 gives for comparison the two leading logarithmic approximations, that in Q^2 of Eq. (2.67) leading to the DGLAP equations and that in $1/x$ from Eq. (3.4), which we will study below. As discussed in Sec. 2.3, the photon virtuality Q determines the transverse size resolution of a DIS experiment, while Bjorken x determines the longitudinal (Ioffe) lifetime

of the partonic fluctuation: we therefore refer to $\ln Q^2$ as the transverse logarithm and to $\ln 1/x$ as the longitudinal logarithm. As one can see from Table 3.1, the two LLA regimes should give identical results when they overlap in the double logarithmic approximation (DLA).

As discussed in the previous chapter, the LLA in Q^2 leads to the evolution described by the DGLAP equations, which allows us to determine the number of partons with transverse size larger than $1/Q$ if we know the number of partons with size larger than $1/Q_0$. Formally speaking, Q_0 is chosen to be large enough that $\alpha_s(Q_0^2) \ll 1$. In x -evolution we hope to find the number of partons of roughly the same transverse size at low x if we know this number at some $x = x_0$. Therefore Fig. 2.22 would have to be modified for small- x evolution. We will return to this subject later, after deriving the linear small- x evolution equation.

Resummation of the leading logarithms of $1/x$ instead of those of Q^2 is the essential paradigm shift needed in studying the small- x asymptotics. The equation resumming leading logarithms of $1/x$ will be, unlike the DGLAP equation, an evolution equation in x not an evolution equation in Q^2 . A main goal of this chapter is to develop the technique of summing such longitudinal logarithmic contributions. We will show that the summation of powers of $\alpha_s \ln 1/x$ leads to gluon distributions increasing as a power of $1/x$ at small x , namely as $(1/x)^{1+\text{const}\alpha_s}$. For hadron-hadron scattering cross sections, $\ln 1/x$ is replaced by $\ln s$ (cut off by some dimensionful scale), so that the resummation of longitudinal logarithms gives cross sections growing as a power of the center-of-mass energy: $\sigma_{tot} \sim s^{1+\text{const}\alpha_s}$.

3.2 Two-gluon exchange: the Low-Nussinov pomeron

We start our analysis of high energy scattering with the lowest-order diagrams. As mentioned earlier, in this chapter we will be using the usual Feynman diagram technique. For simplicity let us consider the high energy scattering of two quark-antiquark bound states (quarkonia) on each other. We assume that the quarkonia either resulted from a splitting of virtual photons of high virtuality Q ($\gamma^* + \gamma^*$ scattering) or consist of quarks sufficiently heavy to insure the applicability of perturbative QCD methods.

Before we start the calculation let us formulate a general rule for high energy scattering, which will be confirmed by explicit calculations below, albeit for the particular case of gluons. Consider a high energy scattering event in which a particle of spin j is exchanged in the t -channel between some scatterers, as shown in Fig. 3.1. The rule is simple: if one wants to count the powers of the center-of-mass energy squared s in the total scattering cross section then the contribution of each t -channel exchange of particle with spin j to the scattering cross section is (Regge 1959, 1960)¹

$$s^{j-1}. \quad (3.5)$$

To avoid confusion between contributions to the scattering amplitude and to the cross section we note that in our (standard) normalization the cross section is $\sigma \sim |M|^2/s^2$, where

¹ This simple rule applies only to counting powers of s and cannot be used to count the powers of $\ln s$, which is a much slower function of s than a power and is therefore neglected by the rule.

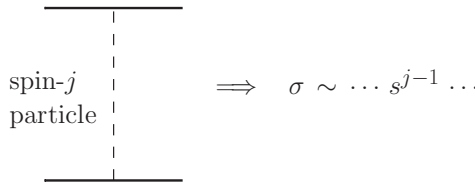


Fig. 3.1. A t -channel exchange of a particle with spin j between two particles scattering at high energy. The exchange shown is assumed to be part of some amplitude squared contributing to the scattering cross section. The contribution of each particle exchange to the resulting scattering cross section is s^{j-1} .

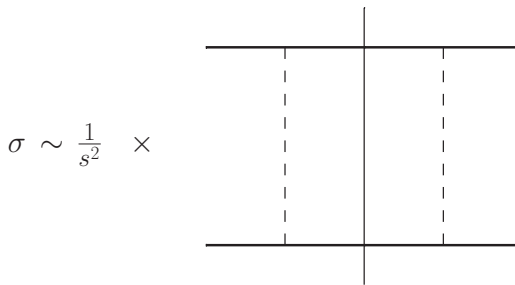


Fig. 3.2. The scattering cross section as the amplitude squared of the t -channel exchange diagram from Fig. 3.1 divided by the appropriate kinematic factors, including s^2 . The vertical solid line denotes the final-state cut.

M is the scattering amplitude (see e.g. Amsler *et al.* (2008)). An exchange of k particles of spin j in the amplitude and k particles in the complex conjugate amplitude leads to a cross section scaling as $\sigma \sim s^{(j-1)2k}$, while the amplitude with k exchanged particles would then scale as $M \sim s^{1+(j-1)k}$. Hence one-particle exchange contributes s^j to the amplitude ($k = 1$), while the exchange of two particles ($k = 2$) gives a factor s^{2j-1} in the amplitude, etc.

As an example, consider the contribution of the squared amplitude in Fig. 3.1 to the total scattering cross section, as shown in Fig. 3.2. According to the above rule the cross section receives contributions from the exchanges of two t -channel particles of spin j , each contributing s^{j-1} . The resulting scattering cross section scales as

$$\sigma \sim s^{2(j-1)}. \tag{3.6}$$

Thus, if the particles exchanged in the t -channel were gluons with spin $j = 1$, the cross section would scale as

$$\sigma_{gluons} \sim s^0. \tag{3.7}$$

On the basis of rule (3.6) we would expect the cross section due to a two-gluon exchange to be constant with energy. This is an important observation, which we will soon verify by explicit calculations.

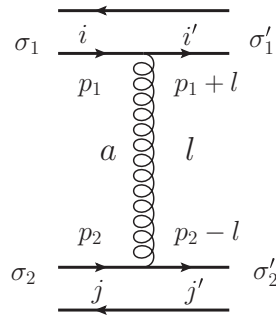


Fig. 3.3. Onium–onium high energy scattering amplitude at leading order. The arrows on the quark lines denote the directions of both the particle number flow and the momentum flow.

Alternatively, if the particles exchanged in the t -channel in Fig. 3.2 were quarks with spin $j = 1/2$ then the cross section would scale as

$$\sigma_{quarks} \sim \frac{1}{s} \quad (3.8)$$

and would decrease with energy. We see that, according to the above rule, the gluon contribution to the scattering cross section dominates the quark contribution. This conclusion is certainly in line with our earlier observation in Sec. 2.4.6 that the gluon distribution dominates in DIS at small x . We see that in high energy processes gluons play a more important role than quarks.

Let us consider the case when scalar particles are exchanged in the t -channel of Fig. 3.2 (we are now going beyond QCD and are considering a scalar theory). The cross section would scale as

$$\sigma_{scalars} \sim \frac{1}{s^2} \quad (3.9)$$

and is also, like the cross section for quark exchanges, small at high energy.

Finally, if spin-2 particles, such as gravitons, are exchanged in the t -channel of Fig. 3.2 then one gets

$$\sigma_{gravitons} \sim s^2 \quad (3.10)$$

and the cross section would grow rather fast with energy. Luckily, despite this energy enhancement, gravity is rather weakly coupled at the energies of modern-day accelerators and does not contribute significantly to the total cross sections.

Let us now return to QCD and to the high energy scattering of two quarkonia (to which we will often simply refer to as “onia”). In view of the above rule, and as can be shown by a simple calculation, at high energy the dominant lowest-order contribution to the QCD scattering amplitude is due to a t -channel gluon exchange, as shown in Fig. 3.3.

We are working in the center-of-mass frame, where the top onium (along with its quark and antiquark) in Fig. 3.3 has a large plus light cone component of momentum, while

the lower onium has a large minus momentum component. Specifically, for simplicity neglecting the quark masses one may choose the incoming quarks in Fig. 3.3 to be light-like:

$$p_1^\mu = (p_1^+ \equiv P^+ = \sqrt{s}, 0, 0_\perp) \quad \text{and} \quad p_2^\mu = (0, p_2^- \equiv P^- = \sqrt{s}, 0_\perp), \quad (3.11)$$

using the (+, −, ⊥) notation. Note that, in our high energy kinematics, P^+ and P^- are the two largest momentum scales in the problem; all other momenta are assumed to be much smaller than P^+ and P^- . This is known as the *eikonal approximation*.

A simple calculation in the covariant (Feynman) gauge yields the amplitude for the diagram in Fig. 3.3:

$$iM_{qq \rightarrow qq}^0 = -ig^2 (t^a)_{i'i} (t^a)_{j'j} \frac{1}{l_\perp^2} \bar{u}_{\sigma'_1}(p_1 + l) \gamma^\mu u_{\sigma_1}(p_1) \bar{u}_{\sigma'_2}(p_2 - l) \gamma_\mu u_{\sigma_2}(p_2). \quad (3.12)$$

In arriving at Eq. (3.12) we have used the fact that the outgoing quarks are on mass shell, so that

$$0 = (p_1 + l)^2 = p_1^+ l^- + l^2, \quad (3.13)$$

giving

$$l^- = -\frac{l^2}{p_1^+} = -\frac{l^2}{P^+} \approx 0. \quad (3.14)$$

Similarly

$$l^+ = \frac{l^2}{p_2^-} = \frac{l^2}{P^-} \approx 0 \quad (3.15)$$

and, therefore,

$$l^2 \approx -l_\perp^2. \quad (3.16)$$

We see that in the high energy approximation the exchanged gluon has no longitudinal momentum: we will refer to it as an instantaneous or Coulomb gluon.

To keep only leading powers of P^+ and P^- we use the following trick: we consider that the spinors of the quark line with the large plus momentum (the upper line in Fig. 3.3) are chosen in the Lepage and Brodsky (1980) convention while the spinors in the quark line with the large minus momentum (the lower line in Fig. 3.3) are also chosen in the Lepage and Brodsky (1980) convention but with the P^- and P^+ momenta interchanged (see Eqs. (1.50) and (1.51)). Using Table A.1 in Appendix A we see that γ^+ dominates in the upper quark line of Fig. 3.3 since it carries a large P^+ momentum while γ^- dominates in the lower quark line, which carries a large P^- momentum. With the help of Table A.1 we then obtain²

$$M_{qq \rightarrow qq}^0(\vec{l}_\perp) = -2g^2 (t^a)_{i'i} (t^a)_{j'j} \delta_{\sigma_1 \sigma'_1} \delta_{\sigma_2 \sigma'_2} \frac{s}{l_\perp^2}. \quad (3.17)$$

² One may also use standard notation for Dirac spinors (see e.g. Peskin and Schroeder (1995)). In this case, neglecting l compared to p_1 and p_2 , one should use the relation $\bar{u}_{\sigma'}(p) \gamma^\mu u_\sigma(p) = 2p^\mu \delta_{\sigma\sigma'}$, which follows from the Gordon identity, to simplify Eq. (3.12).

The square of the amplitude in Eq. (3.17) leads to the following high energy cross section:

$$\sigma_{qq \rightarrow qq}^0 = \frac{2\alpha_s^2 C_F}{N_c} \int \frac{d^2 l_\perp}{(l_\perp^2)^2}. \quad (3.18)$$

We see that, in agreement with the rule in Eq. (3.6), the cross section due to two t -channel gluon exchanges is independent of energy at high energy. This feature of QCD was first noticed by Low (1975) and Nussinov (1976). The two t -channel gluon exchange cross section is sometimes called the *Low–Nussinov pomeron*, since this result was the first successful attempt to describe hadronic cross sections in the framework of perturbative QCD: in pre-QCD language hadronic cross sections were described as being due to the t -channel exchange of a hypothetical particle with the quantum numbers of the vacuum called *the pomeron*, named after I. Y. Pomeranchuk (1958). The contribution of the pomeron to the scattering amplitude is

$$M \sim s^{\alpha(t)}, \quad (3.19)$$

where s and t are Mandelstam variables and $\alpha(t)$ is the “angular momentum” of the pomeron, usually referred to as the *pomeron trajectory*. The contribution of a single pomeron exchange to the total cross section is

$$\sigma_{tot} \sim s^{\alpha(0)-1}. \quad (3.20)$$

Here $\alpha(0)$ is the value of the pomeron trajectory at $t = 0$, which is the point where it intercepts the angular momentum axis in the (t, α) -plane. Therefore $\alpha(0)$ is referred to as the *pomeron intercept* and is sometimes denoted by α_P . As one can see from Eq. (3.20), the pomeron intercept always comes in the combination $\alpha(0) - 1$: according to a common notation, we will often refer to $\alpha(0) - 1 = \alpha_P - 1$ as itself the pomeron intercept. Frequently one uses a linear expansion of the pomeron trajectory near $t = 0$:

$$\alpha(t) \approx \alpha(0) + \alpha' t. \quad (3.21)$$

The parameter α' is called the *slope* of the pomeron trajectory. A tantalizing feature of strong interactions is that the linear approximation (3.21) actually describes the pomeron trajectory $\alpha(t)$ rather well at all values of t . This observation gave rise to the development of string theory, which started out as a candidate theory for strong interactions (see e.g. Green, Schwarz, and Witten (1987)).

From Eq. (3.18) it is clear that the Low–Nussinov pomeron has intercept $\alpha(0) - 1 = 0$. In high energy proton–proton (pp) (and proton–antiproton, $p\bar{p}$) collisions, analysis of the experimental data showed that the total cross section grows approximately as follows (Donnachie and Landshoff 1992):

$$\sigma_{tot}^{pp} \sim s^{0.08}. \quad (3.22)$$

That is, using pre-QCD language, the pomeron intercept $\alpha_P - 1 = 0.08$. Since soft non-perturbative QCD physics is probably responsible for much of the total pp cross section observed at many modern-day accelerators, the pomeron with intercept $\alpha_P - 1 = 0.08$ is usually called the “soft pomeron”.

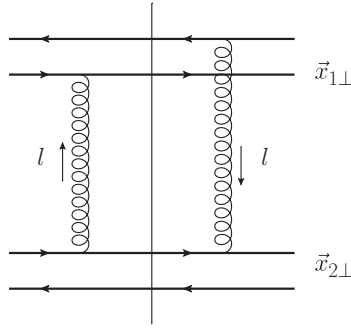


Fig. 3.4. A diagram contributing to the onium–onium high energy scattering cross section at leading order. The arrows next to the gluon lines indicate the direction of momentum flow and the vertical straight line denotes the final state cut.

We see that the prediction of Low and Nussinov that $\alpha_P - 1 = 0$, while it does not give the correct pomeron intercept, is not far from it, in the sense of giving a cross section that at least does not decrease with energy. (Of course there is no *a priori* reason to expect a perturbative calculation to describe the total pp scattering cross section, but it is good to have at least qualitative agreement between the two.) As we will see below, higher-order perturbative corrections to the cross section (3.18) generate a positive order- α_s contribution to the $\alpha_P - 1 = 0$ result. Note that the fact that experimental measurement of the total pp scattering cross section (3.22) gives a result that does not fall off with energy but instead rises slowly with s , when combined with the above rule for counting powers of s (see (3.6)), demonstrates that there must exist a spin-1 particle responsible for strong interactions – the gluon. This is exactly the argument for the existence of gluons mentioned in Sec. 1.1.

The l_\perp -integral in Eq. (3.18) has an infrared (IR) divergence. This is natural since we are calculating a cross section for the scattering of free color charges (quarks). To make the cross section IR-finite we need to remember that the scattering quarks are part of the onium wave functions. Suppose that the $q\bar{q}$ pairs have separations $\vec{x}_{1\perp}$ and $\vec{x}_{2\perp}$ in transverse coordinate space, though the impact parameter between the two onia has been integrated out. By summing diagrams with all possible gluon connections to quarks and antiquarks, one of which is shown in Fig. 3.4, one can then show that the total onium–onium scattering cross section is

$$\sigma_{tot}^{onium+onium} = \int d^2x_{1\perp} d^2x_{2\perp} \int_0^1 dz_1 dz_2 |\Psi(\vec{x}_{1\perp}, z_1)|^2 |\Psi(\vec{x}_{2\perp}, z_2)|^2 \hat{\sigma}_{tot}^{onium+onium} \quad (3.23)$$

with

$$\hat{\sigma}_{tot}^{onium+onium} = \frac{2\alpha_s^2 C_F}{N_c} \int \frac{d^2l_\perp}{(l_\perp^2)^2} (2 - e^{-i\vec{l}_\perp \cdot \vec{x}_{1\perp}} - e^{i\vec{l}_\perp \cdot \vec{x}_{1\perp}})(2 - e^{-i\vec{l}_\perp \cdot \vec{x}_{2\perp}} - e^{i\vec{l}_\perp \cdot \vec{x}_{2\perp}}), \quad (3.24)$$

at the lowest order in α_s . Here $\Psi(\vec{x}_\perp, z)$ is the onium light cone wave function with quark light cone momentum fraction z . The exact form of the wave function is not important

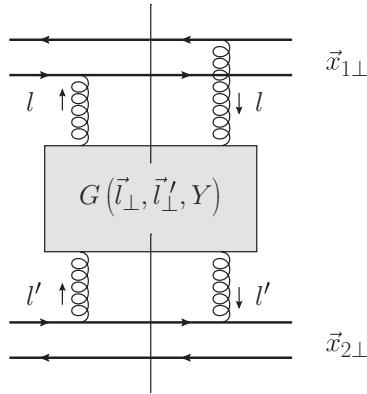


Fig. 3.5. A general representation of the onium–onium scattering cross section at high energy. The rectangle denotes all leading- $\ln s$ corrections to the two-gluon exchange cross section from Fig. 3.5.

for the moment. The summation and averaging over all appropriate quantum numbers is implicit in the $|\Psi|^2$ factors in Eq. (3.23).

The l_\perp -integral in Eq. (3.24) is now finite; if we average over the directions of $\vec{x}_{1\perp}$ and $\vec{x}_{2\perp}$ then it can be easily carried out, giving

$$\langle \hat{\sigma}_{tot}^{onium+onium} \rangle = \frac{4\pi\alpha_s^2 C_F}{N_c} x_{<}^2 \left(\ln \frac{x_{>}}{x_{<}} + 1 \right), \quad (3.25)$$

where $x_{>(<)} = \max(\min)\{|\vec{x}_{1\perp}|, |\vec{x}_{2\perp}|\}$ and $\langle \dots \rangle$ denotes angular averaging.

We will now look for corrections to this lowest-order result.

3.3 The Balitsky–Fadin–Kuraev–Lipatov evolution equation

As discussed in Sec. 3.1, in high energy scattering (or at small Bjorken x) one would like to sum the longitudinal logarithms, i.e., the powers of $\alpha_s \ln s$ (or $\alpha_s \ln 1/x$). We will denote the sum of all such corrections to the Born-level onium–onium scattering cross section found above in Sec. 3.2 by the shaded rectangle in Fig. 3.5.

Generalizing the cross section in Eq. (3.24) we write

$$\hat{\sigma}_{tot}^{onium+onium} = \frac{2\alpha_s^2 C_F}{N_c} \int \frac{d^2 l_\perp d^2 l'_\perp}{l_\perp^2 l'_\perp^2} \left(2 - e^{-i\vec{l}_\perp \cdot \vec{x}_{1\perp}} - e^{i\vec{l}_\perp \cdot \vec{x}_{1\perp}} \right) \times \left(2 - e^{-i\vec{l}'_\perp \cdot \vec{x}_{2\perp}} - e^{i\vec{l}'_\perp \cdot \vec{x}_{2\perp}} \right) G(\vec{l}_\perp, \vec{l}'_\perp, Y), \quad (3.26)$$

where l and l' are the momenta of the gluon lines on each side of the shaded rectangle, as illustrated in Fig. 3.5. We also define the *rapidity* variable $Y = \ln(s|\vec{x}_{1\perp}||\vec{x}_{2\perp}|)$; it is important that $Y \sim \ln s$, though the exact cutoff under the logarithm of the energy is not important in the leading-logarithmic approximation that we would like to apply here. The shaded rectangle in Fig. 3.5 brings in a factor $G(\vec{l}_\perp, \vec{l}'_\perp, Y)$. The lowest-order expression

(3.24) is recovered by substituting

$$G(\vec{l}_\perp, \vec{l}'_\perp, Y=0) = G_0(\vec{l}_\perp, \vec{l}'_\perp) = \delta^2(\vec{l}_\perp - \vec{l}'_\perp) \quad (3.27)$$

in Eq. (3.26).

Below we will construct an equation for $G(\vec{l}_\perp, \vec{l}'_\perp, Y)$ by analyzing the one-gluon order- α_s corrections to Eq. (3.24) and to Fig. 3.4.

3.3.1 Effective emission vertex

Let us start with the real one-gluon corrections to Fig. 3.4, i.e., corrections where the extra gluon is present in the final state (the gluon is cut). The difference between the quark–quark scattering cross section (3.18) and the onium–onium cross section (3.24) is only in the so-called impact factors, which at the lowest order, considered here, are simply factors like $2 - e^{-i\vec{l}_\perp \cdot \vec{x}_{1\perp}} - e^{i\vec{l}'_\perp \cdot \vec{x}_{1\perp}}$; see the large parentheses in Eq. (3.26). Thus we will first consider corrections to the quark–quark high energy scattering amplitude.

All possible real-gluon emission corrections to the quark–quark scattering amplitude of Fig. 3.3 are shown in Fig. 3.6. In order to extract the leading- $\ln s$ contribution we assume that $k^+ \ll P^+$, $k^- \ll P^-$, where k^μ is the momentum of the produced (i.e., final-state) gluon. If one performs the calculation in the covariant (Feynman) gauge then all the diagrams in Fig. 3.6 will contribute (Fadin, Kuraev, and Lipatov 1975). Here we will perform the calculation in the $\eta \cdot A = A^+ = 0$ light cone gauge. The advantage of this gauge is that in it diagrams D and E in Fig. 3.6 do not contribute (at high energy). To see this we again use the same trick and choose the Lepage and Brodsky (1980) convention for spinors for the upper quark line and the same convention with P^- and P^+ interchanged for the lower line. Again with the help of Table A.1, one can see that the dominant contribution of each diagram at high energy comes from the γ^+ 's in the quark–gluon vertices in the upper quark line and from the γ^- 's in the quark–gluon vertices in the lower quark line. (For instance, the numerator of the quark propagator corresponding to the lower line in diagram D gives $(p_2 - q) \cdot \gamma \approx (1/2)p_2^- \gamma^+$, so that, since $(\gamma^+)^2 = 0$, the adjacent vertices can only give either γ^- or γ^\perp ; the γ^\perp contribution is suppressed by powers of P^- , though, leaving only the γ^- vertices.) The polarization vector of the outgoing gluon in the $A^+ = 0$ light cone gauge can be parametrized as

$$\epsilon_\lambda^\mu(k) = \left(0, \frac{2\vec{\epsilon}_\perp^\lambda \cdot \vec{k}_\perp}{k^+}, \vec{\epsilon}_\perp^\lambda \right) \quad (3.28)$$

with transverse vector $\vec{\epsilon}_\perp^\lambda = -(1/\sqrt{2})(\lambda, i)$. We see that the γ^- from the emission vertex of the gluon carrying momentum k in graphs D and E is multiplied by $\epsilon_\lambda^{+*} = 0$ and therefore gives zero. We are left with diagrams A, B, and C to calculate.

Let us start by calculating diagrams B and C. Using the Feynman rules we write for diagram B (note that $\eta^\mu = (0, 2, 0_\perp)$)

$$iM_{qq \rightarrow qqG}^B = g^3 (t^a t^c)_{i'i} (t^c)_{j'j} \bar{u}_{\sigma'_1}(p_1 - k + q) \epsilon_\lambda^*(k) \frac{\not{p}_1 + \not{q}}{(p_1 + q)^2} \gamma^\mu u_{\sigma_1}(p_1) \\ \times \bar{u}_{\sigma'_2}(p_2 - q) \gamma^\nu u_{\sigma_2}(p_2) \frac{-i}{q^2} \left(g_{\mu\nu} - \frac{\eta_\mu q_\nu + \eta_\nu q_\mu}{\eta \cdot q} \right). \quad (3.29)$$

(The colors and polarizations of the incoming and outgoing quarks are labeled in the same way as in Fig. 3.3.) As in the lowest-order case we note that the outgoing quarks are on mass shell, so that $(p_1 - k + q)^2 = 0$ and $(p_2 - q)^2 = 0$. These conditions give

$$q^- = k^- + O\left(\frac{1}{P^+}\right), \quad q^+ = O\left(\frac{1}{P^-}\right). \quad (3.30)$$

We see that $q^2 \approx -\vec{q}_\perp^2$ and, therefore, the gluon with momentum q is an instantaneous (Coulomb) gluon.

Using the Dirac equation we see that the q_ν -term in the large parentheses in Eq. (3.29), which postmultiplies the matrix element $\bar{u}_{\sigma'_2}(p_2 - q) \gamma^\nu u_{\sigma_2}(p_2)$, is zero. The η_ν -term in the gluon propagator of Eq. (3.29) gives $\eta_\nu \bar{u}_{\sigma'_2}(p_2 - q) \gamma^\nu u_{\sigma_2}(p_2) = \bar{u}_{\sigma'_2}(p_2 - q) \gamma^+ u_{\sigma_2}(p_2)$, which, if one uses the Lepage and Brodsky (1980) convention for spinors with the + and - momenta interchanged, is suppressed by $1/P^{-2}$ in comparison with the leading-order term arising from $\bar{u}_{\sigma'_2}(p_2 - q) \gamma^- u_{\sigma_2}(p_2)$. This leaves us with only the $g_{\mu\nu}$ -term within the large parentheses. Therefore $\nu = -$ and $\mu = +$ gives the dominant contribution in the matrix elements in Eq. (3.29). Making the approximations $(p_1 + q) \cdot \gamma \approx (1/2)P^+ \gamma^-$ and $(p_1 + q)^2 \approx P^+ q^-$ in the quark propagator, and using Table A.1 along with Eq. (3.30), yields

$$iM_{qq \rightarrow qqG}^B = 4i g^3 (t^a t^c)_{i'i} (t^c)_{j'j} \delta_{\sigma_1 \sigma'_1} \delta_{\sigma_2 \sigma'_2} \frac{s}{q_\perp^2} \frac{\vec{\epsilon}_\perp^{\lambda*} \cdot \vec{k}_\perp}{k_\perp^2}. \quad (3.31)$$

A similar calculation for diagram C in Fig. 3.6 would readily show that its contribution $M_{qq \rightarrow qqG}^C$ is different from $M_{qq \rightarrow qqG}^B$ in Eq. (3.31) by an overall minus sign and by a change in the order of the color matrices: $t^a t^c \rightarrow t^c t^a$. The sum of the two graphs is

$$M_{qq \rightarrow qqG}^B + M_{qq \rightarrow qqG}^C = -4i g^3 f^{abc} (t^b)_{i'i} (t^c)_{j'j} \delta_{\sigma_1 \sigma'_1} \delta_{\sigma_2 \sigma'_2} \frac{s}{q_\perp^2} \frac{\vec{\epsilon}_\perp^{\lambda*} \cdot \vec{k}_\perp}{k_\perp^2}. \quad (3.32)$$

It is important to note that, for an Abelian theory such as QED, the sum of diagrams B and C would be zero, owing to the absence of color matrices. This makes physical sense: as we will see below in more detail, the high energy approximation used above implies that each quark moves without recoil along its light cone throughout the scattering process. For an electron this would mean that high energy scattering does not affect it at all: it does not acquire any acceleration. Therefore, without acceleration or deceleration the electron will not radiate; this statement is equivalent to the cancellation of graphs B and C in QED. In non-Abelian theories such as QCD, radiation is caused not only by acceleration but also by color rotation. Thus the recoilless motion of the quarks does not mean the absence of radiation: what happens in diagrams B and C in Fig. 3.6 is that the color of the upper quark line is rotated by the t -channel gluon exchange interaction with the lower quark line.

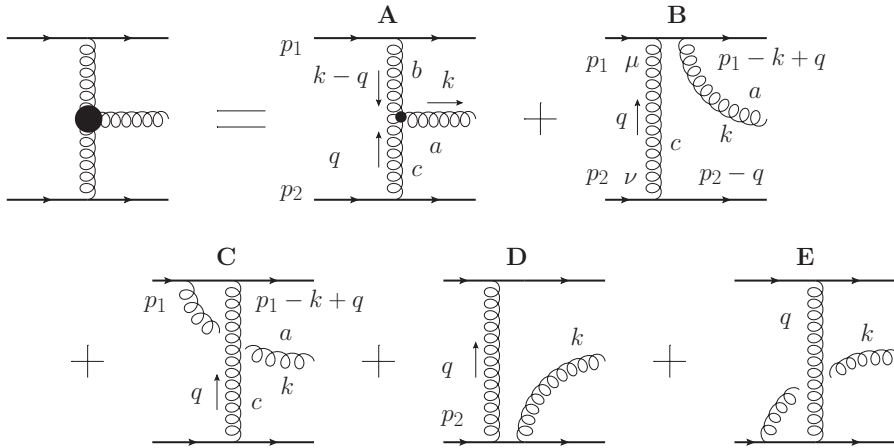


Fig. 3.6. The effective real-gluon emission vertex (the Lipatov vertex), defined as the sum of all gluon emission diagrams. The triple gluon vertex is denoted by the smaller solid circle while the Lipatov vertex is shown by the larger solid circle.

Because of this color flip, diagrams B and C no longer cancel, which means that, unlike in QED, the radiations from the upper quark before (C) and after (B) the interaction do not cancel. Thus, we see that in QCD the gluon radiation can be entirely due to color rotation: this is an essentially non-Abelian feature of the theory.

We now need to calculate the amplitude represented by diagram A in Fig. 3.6. Applying the Feynman rules we write

$$\begin{aligned}
 iM_{qq \rightarrow qqG}^A &= g^3 f^{abc} (t^b)_{i'i} (t^c)_{j'j} \epsilon_{\lambda\rho}^*(k) \bar{u}_{\sigma'_1}(p_1 - k + q) \gamma^{\mu'} u_{\sigma_1}(p_1) \\
 &\times \bar{u}_{\sigma'_2}(p_2 - q) \gamma^{\nu'} u_{\sigma_2}(p_2) \left[(k - 2q)^\rho g^{\mu\nu} + (q - 2k)^\nu g^{\mu\rho} + (q + k)^\mu g^{\nu\rho} \right] \\
 &\times \frac{1}{q^2} \left(g_{\nu\nu'} - \frac{\eta_\nu q_{\nu'} + \eta_{\nu'} q_\nu}{\eta \cdot q} \right) \frac{1}{(k - q)^2} \left(g_{\mu\mu'} - \frac{\eta_\mu (k - q)_{\mu'} + \eta_{\mu'} (k - q)_\mu}{\eta \cdot (k - q)} \right).
 \end{aligned}
 \tag{3.33}$$

(The Lorentz indices, while not explicitly shown in Fig. 3.6A, should be self-evident.) The evaluation proceeds along lines similar to the calculation of graphs B and C. We first note that in the q -line propagator the $q_{\nu'}$ -term is zero by the Dirac equation (current conservation), while the $\eta_{\nu'}$ -term is strongly suppressed at high energy (see Table A.1): this leaves only the $g_{\nu\nu'}$ -term to contribute. As a side observation, we note that the $A^+ = 0$ light cone gauge is equivalent to the covariant (Feynman) gauge for the lower part of the diagrams in Fig. 3.6. This is a useful tool, which we will employ again later.

Again, using Table A.1 and the Lepage and Brodsky (1980) convention for spinors (with + and - momenta interchanged), we see that γ^- gives the leading contribution in the matrix element $\bar{u}_{\sigma'_2}(p_2 - q) \gamma^{\nu'} u_{\sigma_2}(p_2)$. Since in the $A^+ = 0$ light cone gauge we have $\epsilon_\lambda^+ = 0$ and since the propagator of the $k - q$ line is also zero when either of its (upper) indices is +, we conclude that only the $g^{\mu\rho}$ term in the triple-gluon vertex contributes at

high energy. Similarly, γ^+ gives the leading contribution in $\bar{u}_{\sigma'_1}(p_1 - k + q)\gamma^{\mu'}u_{\sigma_1}(p_1)$. Finally, since we have taken care to have the external lines carry the same momenta (and other quantum numbers) in all the graphs in Fig. 3.6, we see that Eq. (3.30) applies for diagram A as well. Applying all the above simplifications, we rewrite Eq. (3.33) as

$$M_{qq \rightarrow qqG}^A = 4ig^3 f^{abc} (t^b)_{i'i} (t^c)_{j'j} \delta_{\sigma_1 \sigma'_1} \delta_{\sigma_2 \sigma'_2} \frac{s}{q_{\perp}^2 (\vec{k}_{\perp} - \vec{q}_{\perp})^2} \vec{\epsilon}_{\perp}^{\lambda*} \cdot (\vec{k}_{\perp} - \vec{q}_{\perp}). \quad (3.34)$$

Adding all the diagrams in Fig. 3.6 yields

$$M_{qq \rightarrow qqG} = 2ig^2 (t^b)_{i'i} (t^c)_{j'j} \delta_{\sigma_1 \sigma'_1} \delta_{\sigma_2 \sigma'_2} \frac{s}{q_{\perp}^2 (\vec{k}_{\perp} - \vec{q}_{\perp})^2} \vec{\epsilon}_{\perp}^{\lambda*} \cdot \vec{\Gamma}_{\perp}^{abc}, \quad (3.35)$$

where we have defined an effective vertex

$$\vec{\Gamma}_{\perp}^{abc} = 2gf^{abc} \left[\vec{k}_{\perp} - \vec{q}_{\perp} - \frac{(\vec{k}_{\perp} - \vec{q}_{\perp})^2}{k_{\perp}^2} \vec{k}_{\perp} \right]. \quad (3.36)$$

The vertex $\vec{\Gamma}_{\perp}^{abc}$ was first derived in Fadin, Kuraev, and Lipatov (1975, 1977). In the literature it is usually referred to as the *Lipatov vertex*. It is pictured on the left-hand side of Fig. 3.6, where it is denoted by the large solid circle. The origin of this notation can be seen in Eq. (3.35), which one can regard as containing the propagators of the two t -channel gluon lines (\vec{q}_{\perp}^2 and $(\vec{k}_{\perp} - \vec{q}_{\perp})^2$), the color factors and Kronecker deltas coming from the quark lines, an overall factor of s characteristic of the leading high energy amplitudes, and the vertex $\vec{\Gamma}_{\perp}^{abc}$. We see that all five diagrams A–E in Fig. 3.6 can be thought of as one diagram with an effective Lipatov vertex $\vec{\Gamma}_{\perp}^{abc}$ instead of the triple-gluon vertex.

We have to add here that there are gauges in which diagrams B through E in Fig. 3.6 do not contribute in the high energy limit, so that the amplitude is simply given by diagram A. An example would be the $A^0 = 0$ gauge.

Squaring the amplitude in Eq. (3.35), we write the corresponding cross section as

$$\sigma_{qq \rightarrow qqG} = \frac{2\alpha_s^3 C_F}{\pi^2} \int \frac{d^2 k_{\perp} d^2 q_{\perp}}{k_{\perp}^2 q_{\perp}^2 (\vec{k}_{\perp} - \vec{q}_{\perp})^2} \int_{\vec{k}_{\perp}^2/P^-}^{P^+} \frac{dk^+}{k^+}. \quad (3.37)$$

As in the derivation of the DGLAP evolution equations in Chapter 2, we obtain a logarithmic longitudinal integral – the integral over k^+ in the above expression. Since Eq. (3.37) was derived in the high energy approximation with $P^+ \gg k^+$, in order to obtain the leading logarithmic ($\ln s$) contribution we put P^+ as the upper limit of the k^+ integral (the same applies to the lower limit of this integral): defining the rapidity of the gluon by³

$$y = \ln \frac{P^-}{k^-}, \quad (3.38)$$

³ The standard rapidity definition is $y = (1/2) \ln(k^+/k^-)$ in the center-of-mass frame. Our definition here is different by an overall shift, making the rapidity equal to zero in the direction of one of the onia and equal to $Y = \ln(s/k_{\perp}^2)$ in the direction of the other.

we rewrite the gluon production cross section as

$$\sigma_{qq \rightarrow qqG} = \frac{2\alpha_s^3 C_F}{\pi^2} \int \frac{d^2 k_\perp d^2 q_\perp}{k_\perp^2 q_\perp^2 (\vec{k}_\perp - \vec{q}_\perp)^2} \int_0^Y dy. \tag{3.39}$$

Here $Y = \ln s/k_\perp^2$ is the total rapidity interval between the colliding quarks; since our goal is to track the leading- $\ln s$ contribution to the cross section, this Y is for us not different from the $Y = \ln(s|\vec{x}_{1,\perp}||\vec{x}_{2,\perp}|)$ defined earlier in the chapter. The difference between the two does not contain $\ln s$ and can be disregarded at degree of our precision. For simplicity, every time we discuss leading- $\ln s$ asymptotics we will assume that $Y = \ln(s/m_\perp^2)$, with m_\perp some transverse momentum scale the exact value of which is irrelevant in the leading- $\ln s$ approximation.

Just as for the quark–quark scattering in Eq. (3.18), the cross section in Eq. (3.37) has IR divergences at $\vec{q}_\perp = 0$ and $\vec{q}_\perp = \vec{k}_\perp$ since we are considering free quark scattering. Generalizing this result to onium–onium scattering by summing over all interactions of quarks and antiquarks, we include the impact factors that regulate these divergences,⁴ obtaining, after relabeling the momenta to match those in Eq. (3.26),

$$\begin{aligned} \hat{\sigma}_{1,real}^{onium+onium} &= \frac{2\alpha_s^2 C_F}{N_c} \int \frac{d^2 l_\perp d^2 l'_\perp}{l_\perp^2 l'^2_\perp} \left(2 - e^{-i\vec{l}_\perp \cdot \vec{x}_{1\perp}} - e^{i\vec{l}_\perp \cdot \vec{x}_{1\perp}} \right) \\ &\quad \times \left(2 - e^{-i\vec{l}'_\perp \cdot \vec{x}_{2\perp}} - e^{i\vec{l}'_\perp \cdot \vec{x}_{2\perp}} \right) G_1^{real}(\vec{l}_\perp, \vec{l}'_\perp, Y), \end{aligned} \tag{3.40}$$

where

$$G_1^{real}(\vec{l}_\perp, \vec{l}'_\perp, Y) = \frac{\alpha_s N_c}{\pi^2} Y \frac{1}{(\vec{l}_\perp - \vec{l}'_\perp)^2}. \tag{3.41}$$

A contribution to Eq. (3.40) is shown in Fig. 3.7; the circles denote Lipatov vertices. (Indeed, one has to sum the diagram in Fig. 3.7 over all connections of t -channel gluons to all quark lines to obtain Eq. (3.40).)

We have made the first step in understanding the structure of the shaded rectangle in Fig. 3.5 by calculating the lowest-order real-emission correction to Fig. 3.4. Our results so far can be written as (see Eqs. (3.26) and (3.27))

$$\begin{aligned} G(\vec{l}_\perp, \vec{l}'_\perp, Y) &= G_0(\vec{l}_\perp, \vec{l}'_\perp) + G_1^{real}(\vec{l}_\perp, \vec{l}'_\perp, Y) + \dots \\ &= G_0(\vec{l}_\perp, \vec{l}'_\perp) + \frac{\alpha_s N_c}{\pi^2} \int_0^Y dy \int \frac{d^2 q_\perp}{(\vec{l}_\perp - \vec{q}_\perp)^2} G_0(\vec{q}_\perp, \vec{l}'_\perp) + \dots \end{aligned} \tag{3.42}$$

While at the moment Eq. (3.42) may seem like a trivial rewriting of Eq. (3.41), it will be useful later.

⁴ The divergence at $k_\perp = 0$ still remains in the real-gluon contribution to the total cross section; it will be discussed further in Chapter 8 when we consider gluon production.

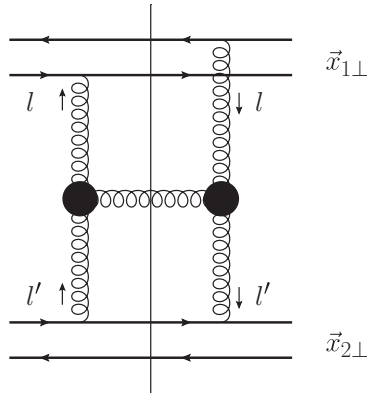


Fig. 3.7. The sum of the real one-gluon corrections to the two-gluon exchange cross section of Fig. 3.4 represented with the help of the effective Lipatov vertices from Fig. 3.6, denoted by the solid circles.

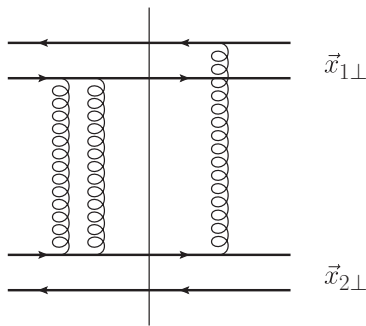


Fig. 3.8. An example of a leading- $\ln s$ order- α_s virtual correction to the Born amplitude.

3.3.2 Virtual corrections and reggeized gluons

To complete our calculation of the order- α_s corrections to the Born-level onium–onium scattering cross section in Eq. (3.24) we need to include the virtual corrections, i.e., diagrams where the extra gluon is not present in the final state. In the amplitude squared we are interested in interference terms between the leading-order single-gluon exchange amplitude of Fig. 3.3 and order- α_s^2 diagrams including one-gluon virtual corrections to it: an example of such a diagram is shown in Fig. 3.8.

Diagrams representing the main types of virtual correction to quark–quark scattering are shown in Fig. 3.9. (All other virtual corrections may be obtained by mirror reflections of the graphs in Fig. 3.9.) As before we assume that all momenta are much smaller than P^+ and P^- .

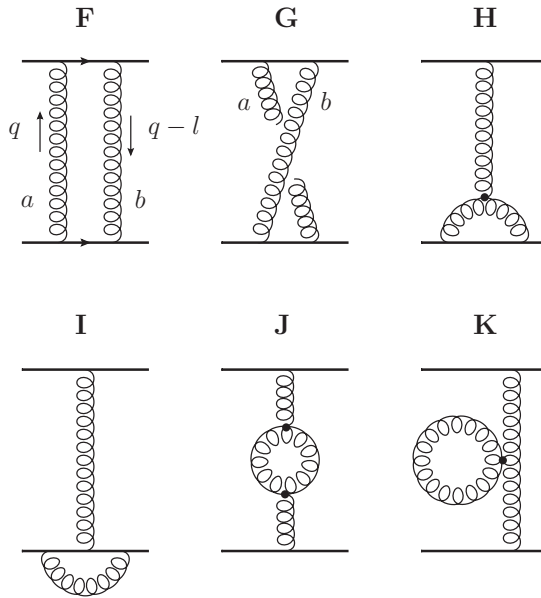


Fig. 3.9. The main classes of the leading-order virtual corrections to the quark–quark scattering amplitude from Fig. 3.3. The small solid circles denote three- and four-gluon vertices.

Our goal is to find the order- α_s^2 amplitude in Fig. 3.9. Instead of a lengthy direct calculation we use the following double-subtracted dispersion relation for scattering amplitudes:⁵

$$M(s, t) = M(s = 0, t) + s \partial_s M(s = 0, t) + \frac{s^2}{\pi} \left[\int_{4m^2}^{\infty} ds' \frac{\text{Im}_s M(s', t)}{s'^2(s' - s)} + \int_{4m^2 - t}^{\infty} du' \frac{\text{Im}_u M(u', t)}{(4m^2 - t - u')^2 (u' - u)} \right] \quad (3.43)$$

where ∂_s denotes a partial derivative with respect to s . The first term in the brackets in Eq. (3.43) contains a discontinuity in the s -channel, while the second term has a discontinuity in the u -channel. (To underscore this, we have relabeled the argument of the amplitude M in the second term to show explicitly its dependence on u and have replaced s' by $4m^2 - t - u'$ in the denominator of the second term.) Above, having in mind the $qq \rightarrow qq$ scattering amplitude, we have assumed here that quarks have a small mass m , such that $4m^2$ is the particle production threshold in both the s - and the u -channel.

We see from Eq. (3.43) that in order to find the order- α_s^2 amplitude in Fig. 3.9 we need the diagrams that have an imaginary part. Therefore we do not need diagrams H–K in Fig. 3.9 since those lead to amplitudes that are purely real (they cannot be cut). The amplitudes given by diagrams F and G have s - and u -channel discontinuities correspondingly. Denoting them

⁵ The dispersion relations used here are derived in Appendix B. Their derivation can also be found in Forshaw and Ross (1997), in Collins, P. D. B. (1977), and, in a slightly different form, in Weinberg (1996).

$M_{qq \rightarrow qq}^F$ and $M_{qq \rightarrow qq}^G$ we note that, owing to the optical theorem, in the forward scattering case we would have (see e.g. Peskin and Schroeder (1995))

$$\text{Im } M_{qq \rightarrow qq}^F(\text{forward}) = s \sigma_{qq \rightarrow qq}^0; \tag{3.44}$$

here we have averaged over the incoming quarks' quantum numbers in the forward amplitude. The cross section $\sigma_{qq \rightarrow qq}^0$ was calculated above and is given by Eq. (3.18). The scattering in Fig. 3.9 is not forward but we can easily correct Eq. (3.44) for that and write

$$\text{Im } M_{qq \rightarrow qq}^F = \int \frac{d^2 q_\perp}{(4\pi)^2 s} \sum M_{qq \rightarrow qq}^0(\vec{q}_\perp) \left[M_{qq \rightarrow qq}^0(\vec{q}_\perp - \vec{l}_\perp) \right]^*, \tag{3.45}$$

where the sum runs over the colors and polarizations of the internal quark lines in graph F and \vec{l}_\perp is the net momentum transfer between the quarks, as shown in Fig. 3.9. Working in the covariant ($\partial_\mu A^\mu = 0$) Feynman gauge we substitute the one-gluon exchange amplitude $M_{qq \rightarrow qq}^0(\vec{q}_\perp)$ from Eq. (3.17) into Eq. (3.45), obtaining

$$\text{Im } M_{qq \rightarrow qq}^F = 4\alpha_s^2 (t^b t^a)_{i'i} (t^b t^a)_{j'j} \delta_{\sigma_1 \sigma_1'} \delta_{\sigma_2 \sigma_2'} \int \frac{d^2 q_\perp}{q_\perp^2 (\vec{q}_\perp - \vec{l}_\perp)^2} s. \tag{3.46}$$

(Here the colors and helicities of the external quark lines are labeled in the same way as in Eq. (3.17) and as shown in Fig. 3.3.)

The imaginary part of the amplitude $M_{qq \rightarrow qq}^G$ is obtained from $\text{Im } M_{qq \rightarrow qq}^F$ by interchanging s and u and the color indices a and b along one quark line:

$$\text{Im } M_{qq \rightarrow qq}^G = 4\alpha_s^2 (t^b t^a)_{i'i} (t^a t^b)_{j'j} \delta_{\sigma_1 \sigma_1'} \delta_{\sigma_2 \sigma_2'} \int \frac{d^2 q_\perp}{q_\perp^2 (\vec{q}_\perp - \vec{l}_\perp)^2} u. \tag{3.47}$$

Substituting Eqs. (3.46) and (3.47) into Eq. (3.43), we find the total order- α_s^2 amplitude for $qq \rightarrow qq$ scattering:

$$\begin{aligned} & M_{qq \rightarrow qq}^1(s, t = -l_\perp^2) \\ &= M_{qq \rightarrow qq}^1(s = 0, t) + s \partial_s M_{qq \rightarrow qq}^1(s = 0, t) + \frac{4\alpha_s^2 s^2}{\pi} \delta_{\sigma_1 \sigma_1'} \delta_{\sigma_2 \sigma_2'} \int \frac{d^2 q_\perp}{q_\perp^2 (\vec{q}_\perp - \vec{l}_\perp)^2} (t^b t^a)_{i'i} \\ & \quad \times \left[(t^b t^a)_{j'j} \int_{4m^2}^\infty \frac{ds'}{s'(s' - s)} + (t^a t^b)_{j'j} \int_{4m^2 - t}^\infty \frac{du'}{(4m^2 - t - u')^2 (u' - u)} \right]. \tag{3.48} \end{aligned}$$

Note that the s' -integral in Eq. (3.48) is divergent for $s > 4m^2$ owing to a singularity at $s' = s$ and should be understood as the $\epsilon \rightarrow 0$ limit of the regulated expression obtained by replacing s by $s + i\epsilon$ in it and integrating. The u' -integral is regulated in a similar way.

We require the high energy asymptotics of the amplitude $M_{qq \rightarrow qq}^1(s, t)$. Moreover, we need the leading- $\ln s$ contribution; noting that at high energy $u \approx -s$ and neglecting $s' \ll s$ and $4m^2 - t \ll u' \ll |u|$, while cutting off the s' -integral by s and the u' -integral by $|u| \approx s$

in the UV to obtain the leading logarithms of s , yields

$$M_{qq \rightarrow qq}^1(s, t = -l_\perp^2) = -\frac{4\alpha_s^2 s}{\pi} \delta_{\sigma_1 \sigma'_1} \delta_{\sigma_2 \sigma'_2} \int \frac{d^2 q_\perp}{q_\perp^2 (\vec{q}_\perp - \vec{l}_\perp)^2} \times (t^b t^a)_{i'i} \left[(t^b t^a)_{j'j} \ln \left(\frac{-s}{4m^2} \right) - (t^a t^b)_{j'j} \ln \left(\frac{s}{4m^2 - t} \right) \right]. \quad (3.49)$$

The factor $\ln(-s)$ arises from the exact integration over s' in (3.48); it reflects the fact that this amplitude has a branch cut at $s > 0$. (Note that integration over u' does not lead to such singularities.) In arriving at Eq. (3.49) we have dropped $M_{qq \rightarrow qq}^1(s = 0, t) + s \partial_s M_{qq \rightarrow qq}^1(s = 0, t)$, since these terms grow with energy as at most s , which is subleading compared with the $s \ln s$ scaling of the leading part of the term that we have kept on the right-hand side of Eq. (3.49).

We see from Eq. (3.49) that, as in real-gluon emission, the only reason why the diagrams F and G do not cancel is the presence of color factors: in QED the leading logarithms of energy would vanish for graphs F and G taken together. Keeping $\ln s \sim Y$ terms only we obtain

$$M_{qq \rightarrow qq}^1 = \frac{2\alpha_s^2 N_c s}{\pi} (t^a)_{i'i} (t^a)_{j'j} \delta_{\sigma_1 \sigma'_1} \delta_{\sigma_2 \sigma'_2} \int \frac{d^2 q_\perp}{q_\perp^2 (\vec{q}_\perp - \vec{l}_\perp)^2} Y. \quad (3.50)$$

Note that the color factors have become the same as for the single-gluon exchange amplitude (3.17): we see that the two exchanged gluons in diagrams F and G are in the *color octet* state. We also see that when the two t -channel gluons are in the color singlet state, as in Fig. 3.4 and Eq. (3.24), no logarithms of the energy are generated, whereas when the two gluons are in the color octet state one gets a $\ln s$ contribution, as we have just seen.

Comparing Eq. (3.50) and Eq. (3.17) we can rewrite the former as

$$M_{qq \rightarrow qq}^1(\vec{l}_\perp) = M_{qq \rightarrow qq}^0(\vec{l}_\perp) \omega_G(l_\perp) Y, \quad (3.51)$$

where we have defined the *gluon Regge trajectory*

$$\omega_G(l_\perp) = -\frac{\alpha_s N_c}{4\pi^2} \int d^2 q_\perp \frac{l_\perp^2}{q_\perp^2 (\vec{q}_\perp - \vec{l}_\perp)^2}. \quad (3.52)$$

One can show further that virtual corrections to the amplitude in Eq. (3.17) that are of higher order in α_s , bringing in leading logarithms of s , lead to a simple exponentiation of the result (3.51), so that one can replace the gluon propagator (3.17) by (Fadin, Kuraev, and Lipatov 1975, 1976, 1977; see Sec. 3.3.5 below)

$$\frac{i g_{\mu\nu}}{l_\perp^2} \rightarrow \frac{i g_{\mu\nu}}{l_\perp^2} e^{\omega_G(l_\perp) Y} \sim \frac{i g_{\mu\nu}}{l_\perp^2} s^{\omega_G(l_\perp)}. \quad (3.53)$$

As discussed in Section 3.2, the propagator (3.53) can be viewed as describing the exchange of a particle with spin $j = 1 + \omega_G(l_\perp)$. We will refer to this “quasi-particle” as a *reggeized gluon*. It is given by the sum of all leading- $\ln s$ virtual corrections to a single-gluon exchange and is illustrated in Fig. 3.10. We will denote reggeized gluons by a thick corkscrew line, as shown in Fig. 3.10.

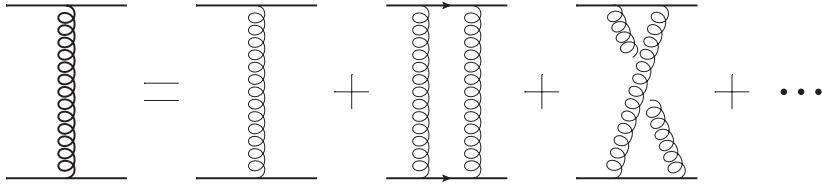


Fig. 3.10. Reggeized gluon (bold corkscrew line) represented as the sum of all leading- $\ln s$ corrections to the single-gluon exchange amplitude for $qq \rightarrow qq$ scattering.

To find the order- α_s virtual correction to the two-gluon exchange cross section, we have to consider the interference between the lowest-order amplitude in Fig. 3.3 and the amplitude in Fig. 3.9:

$$M_{qq \rightarrow qq}^1 (M_{qq \rightarrow qq}^0)^* + M_{qq \rightarrow qq}^0 (M_{qq \rightarrow qq}^1)^* = |M_{qq \rightarrow qq}^0|^2 2\omega_G(l_\perp)Y. \tag{3.54}$$

The correction contributing to the shaded rectangle in Fig. 3.5 is then

$$G_1^{virtual}(\vec{l}_\perp, \vec{l}'_\perp, Y) = G_0(\vec{l}_\perp, \vec{l}'_\perp) 2\omega_G(l_\perp)Y. \tag{3.55}$$

Equation (3.55) resums diagrams like that shown in Fig. 3.8. Using (3.55) we can now include all order- α_s corrections in Eq. (3.42), turning it into

$$G(\vec{l}_\perp, \vec{l}'_\perp, Y) = G_0(\vec{l}_\perp, \vec{l}'_\perp) + \frac{\alpha_s N_c}{\pi^2} \int_0^Y dy \int \frac{d^2 q_\perp}{(\vec{l}_\perp - \vec{q}_\perp)^2} \times \left[G_0(\vec{q}_\perp, \vec{l}'_\perp) - \frac{l_\perp^2}{2q_\perp^2} G_0(\vec{l}_\perp, \vec{l}'_\perp) \right] + O(\alpha_s^2). \tag{3.56}$$

We will now discuss how to generalize this result to all orders in α_s .

3.3.3 The BFKL equation

The shaded rectangle in Fig. 3.5 can be written as a sum of gluon corrections order by order in α_s :

$$G(\vec{l}_\perp, \vec{l}'_\perp, Y) = \sum_{m=0}^\infty G_m(\vec{l}_\perp, \vec{l}'_\perp, Y), \tag{3.57}$$

where each G_m is of order α_s^m , where α_s is the coupling constant. One can readily see that Eq. (3.56) represents the first (order- α_s) iteration for the solution of the following equation:

$$\frac{\partial G(\vec{l}_\perp, \vec{l}'_\perp, Y)}{\partial Y} = \frac{\alpha_s N_c}{\pi^2} \int \frac{d^2 q_\perp}{(\vec{l}_\perp - \vec{q}_\perp)^2} \left[G(\vec{q}_\perp, \vec{l}'_\perp, Y) - \frac{l_\perp^2}{2q_\perp^2} G(\vec{l}_\perp, \vec{l}'_\perp, Y) \right] \tag{3.58}$$

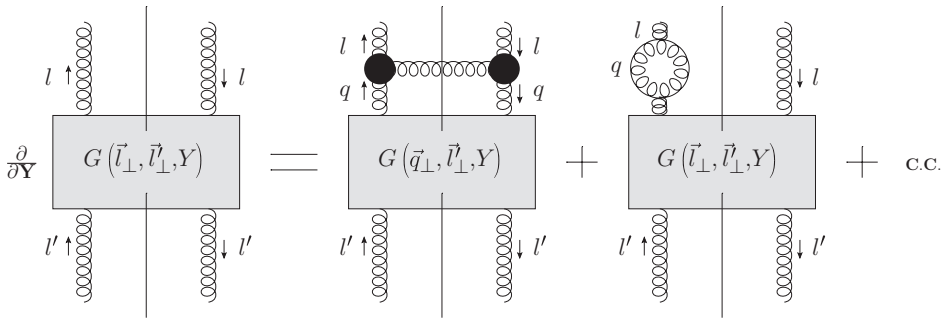


Fig. 3.11. Diagrammatic representation of the BFKL evolution equation (3.58). The second diagram on the right-hand side represents virtual corrections; c.c. denotes the complex conjugate contribution.

with initial condition

$$G(\vec{l}_\perp, \vec{l}'_\perp, Y = 0) = \delta^2(\vec{l}_\perp - \vec{l}'_\perp). \tag{3.59}$$

In fact, as was shown by Fadin, Kuraev, and Lipatov (1977) and by Balitsky and Lipatov (1978), Eq. (3.58) correctly resums all leading- $\ln s$ corrections to the Born-level onium–onium scattering amplitude of Fig. 3.4. This is the Balitsky–Fadin–Kuraev–Lipatov (BFKL) evolution equation (Fadin, Kuraev, and Lipatov 1977, Balitsky and Lipatov 1978). The object $G(\vec{l}_\perp, \vec{l}'_\perp, Y)$ is called the Green function of the BFKL equation: it describes the propagation of two t -channel gluons over the rapidity interval Y .

The BFKL equation for the Green function $G(\vec{l}_\perp, \vec{l}'_\perp, Y)$ is represented graphically in Fig. 3.11. It shows that in one step of BFKL evolution the Green function gets corrected either by real-gluon emissions (summarized in the first diagram on the right-hand side by the square of a Lipatov vertex) or by virtual corrections on either of the two t -channel gluon lines (represented by the second diagram on the right-hand side of Fig. 3.11 together with its complex conjugate). Iterations of the corrections shown in Fig. 3.11 lead to the representation of BFKL evolution by “ladder” diagrams such as those shown in Fig. 3.12.

By performing the calculation at order α_s^3 of the onium–onium scattering amplitude we have obtained two main ingredients that describe high energy scattering in the leading- $\ln s$ approximation: the reggeized gluon and the new effective (Lipatov) vertex of Eq. (3.36). Fadin, Kuraev, and Lipatov (1975, 1976, 1977) proved that the general diagram contributing to the high energy amplitude at the leading- $\ln s$ level can be written as a sum over the produced gluons of the simple ladder-type diagram shown in Fig. 3.12. In this diagram, each vertex is of the type (3.36), each t -channel gluon is a reggeized gluon with propagator (3.53), while all the produced (s -channel) gluons are the regular gluons of the QCD Lagrangian. We are not going to reproduce here the original proof of the BFKL equation. Instead we will rederive this equation in the next chapter in a more rigorous way using LCPT: for a complete derivation using the conventional techniques outlined here we refer the reader to Lipatov (1997, 1999), Del Duca (1995), or Forshaw and Ross (1997).

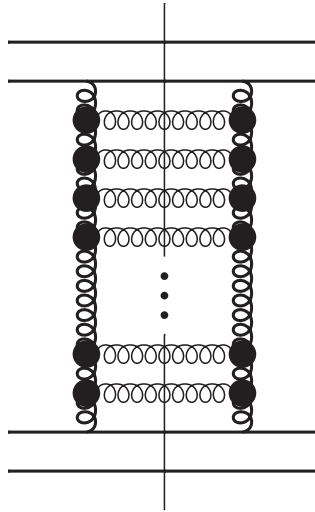


Fig. 3.12. Representation of BFKL evolution as a ladder diagram with effective Lipatov vertices (large solid circles) and reggeized gluons (bold corkscrew lines).

Comparing Fig. 3.12 with Fig. 2.25 we see that both the DGLAP and the BFKL equations effectively resum ladder diagrams, though the “rungs” of the two ladders and the vertices should be understood differently. (Of course, Fig. 2.25 was used to illustrate DLA DGLAP, which is contained in BFKL evolution, as we will shortly see: however, a general DGLAP evolution can also be represented by a ladder diagram resulting from iteration of the DGLAP splitting functions. Unlike the BFKL ladder, the DGLAP ladder would include quarks.) Another major difference between the DGLAP and BFKL ladders is the kinematics of the produced partons. As we saw in Eq. (2.72), the partons in DGLAP evolution are strongly ordered in their transverse momenta, while there is no ordering in their longitudinal momenta. In the BFKL case the kinematics is opposite: it is the longitudinal momenta that are strongly ordered, while there are no constraints on the transverse momenta. One can see this from our derivation of one iteration of the BFKL equation, presented above: we assumed that the plus components of the momenta of all gluons in Figs. 3.6 and 3.9 are much smaller than P^+ , while the minus components are much smaller than P^- . At the same time we did not impose any constraints on the transverse momenta of the gluons in Figs. 3.6 and 3.9. If the momenta of the gluons in the ladder are labeled $k_1^\mu, k_2^\mu, \dots, k_n^\mu$ (as shown in Fig. 3.13), the BFKL kinematics corresponds to

$$P^+ \gg k_1^+ \gg k_2^+ \gg \dots \gg k_n^+, \tag{3.60a}$$

$$k_1^- \ll k_2^- \ll \dots \ll k_n^- \ll P^-, \tag{3.60b}$$

$$k_{1\perp} \sim k_{2\perp} \sim \dots \sim k_{n\perp}. \tag{3.60c}$$

The kinematics in Eqs. (3.60) is known as the *multi-Regge kinematics* and is also sometimes referred to as the multi-peripheral model. It is illustrated by Fig. 3.13. Since the first two

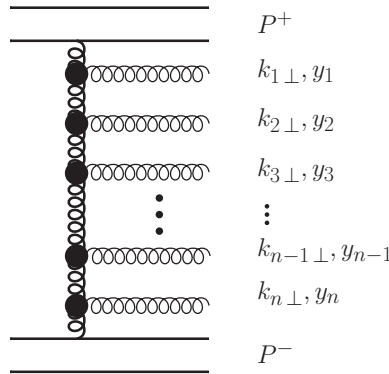


Fig. 3.13. A scattering amplitude the square of which gives the BFKL ladder diagram of Fig. 3.12. The produced gluons have multi-Regge kinematics.

of Eqs. (3.60) imply in terms of rapidities that

$$Y \gg y_1 \gg y_2 \gg \dots \gg y_n \gg 0, \tag{3.61}$$

where y_i , the rapidity of the i th produced gluon, is defined in Eq. (3.38), we see that the multi-Regge kinematics corresponds to the situation where the produced gluons uniformly cover the whole available rapidity interval. Note that owing to this property, the BFKL approach gives us the possibility to calculate the exclusive production cross section for any given number of gluons in the multi-Regge kinematics.

To better understand the dynamics resulting from the BFKL evolution, let us now find the solution of the BFKL equation.

3.3.4 Solution of the BFKL equation

To find the general solution of Eq. (3.58) we need to find eigenfunctions of its integral kernel K_{BFKL} , defined by

$$\int d^2q_{\perp} K_{BFKL}(l, q) f(\vec{q}_{\perp}) \equiv \frac{1}{\pi} \int \frac{d^2q_{\perp}}{(\vec{l}_{\perp} - \vec{q}_{\perp})^2} \left[f(\vec{q}_{\perp}) - \frac{l_{\perp}^2}{2q_{\perp}^2} f(\vec{l}_{\perp}) \right] \tag{3.62}$$

for an arbitrary function $f(\vec{q}_{\perp})$. The BFKL kernel (3.62) is conformally invariant. Therefore, one would expect that its set of eigenfunctions consists of powers of the transverse momentum times the complex exponentials of an integer number multiplying the azimuthal angle:

$$l_{\perp}^{2(\gamma-1)} e^{in\phi_l} \tag{3.63}$$

with γ an arbitrary complex number (analogous to the DGLAP anomalous dimension). Here ϕ_l is the angle between the vector \vec{l}_{\perp} and some chosen axis in the transverse plane, and n is an integer. To see that the functions in Eq. (3.63) are indeed BFKL eigenfunctions

we need to find the action of the BFKL kernel on these functions, that is, we need to evaluate

$$\int d^2q_{\perp} K_{BFKL}(l, q) q_{\perp}^{2(\gamma-1)} e^{in\phi_q} = \frac{1}{\pi} \int \frac{d^2q_{\perp}}{(\vec{l}_{\perp} - \vec{q}_{\perp})^2} \left[q_{\perp}^{2(\gamma-1)} e^{in\phi_q} - \frac{l_{\perp}^2}{2q_{\perp}^2} l_{\perp}^{2(\gamma-1)} e^{in\phi_l} \right]. \tag{3.64}$$

Note that the BFKL equation (3.58) has IR singularities both in the real (first) and virtual (second) terms on its right-hand side. Indeed, the first term is singular at $\vec{q}_{\perp} = \vec{l}_{\perp}$, while the second is singular both at $\vec{q}_{\perp} = \vec{l}_{\perp}$ and at $\vec{q}_{\perp} = 0$. As can also be seen from Eq. (3.58) the singularities cancel each other, making the result of the integration IR-finite.

To evaluate (3.64) we first note that⁶

$$\frac{1}{q_{\perp}^2 (\vec{l}_{\perp} - \vec{q}_{\perp})^2} = \frac{1}{q_{\perp}^2 [q_{\perp}^2 + (\vec{l}_{\perp} - \vec{q}_{\perp})^2]} + \frac{1}{(\vec{l}_{\perp} - \vec{q}_{\perp})^2 [q_{\perp}^2 + (\vec{l}_{\perp} - \vec{q}_{\perp})^2]}, \tag{3.65}$$

so that we obtain, using the substitution $\vec{q}_{\perp} \rightarrow \vec{l}_{\perp} - \vec{q}_{\perp}$ in the first term,

$$\int \frac{d^2q_{\perp}}{q_{\perp}^2 (\vec{l}_{\perp} - \vec{q}_{\perp})^2} = 2 \int \frac{d^2q_{\perp}}{(\vec{l}_{\perp} - \vec{q}_{\perp})^2 [q_{\perp}^2 + (\vec{l}_{\perp} - \vec{q}_{\perp})^2]}. \tag{3.66}$$

After a little more algebra Eq. (3.64) can be written as

$$\int d^2q_{\perp} K_{BFKL}(l, q) q_{\perp}^{2(\gamma-1)} e^{in\phi_q} = \frac{1}{\pi} \int d^2q_{\perp} \left\{ \frac{q_{\perp}^{2(\gamma-1)} e^{in\phi_q}}{(\vec{l}_{\perp} - \vec{q}_{\perp})^2} - \frac{l_{\perp}^{2\gamma} e^{in\phi_l}}{q_{\perp}^2} \left[\frac{1}{(\vec{l}_{\perp} - \vec{q}_{\perp})^2} - \frac{1}{q_{\perp}^2 + (\vec{l}_{\perp} - \vec{q}_{\perp})^2} \right] \right\}. \tag{3.67}$$

Taking $l_{\perp}^{2(\gamma-1)} e^{in\phi_l}$ outside the integral we obtain

$$\int d^2q_{\perp} K_{BFKL}(l, q) q_{\perp}^{2(\gamma-1)} e^{in\phi_q} = \chi(n, \gamma) l_{\perp}^{2(\gamma-1)} e^{in\phi_l}, \tag{3.68}$$

where

$$\chi(n, \gamma) = \int_0^{\infty} dt \left[\frac{1}{2\pi} \int_0^{2\pi} \frac{d\phi_q}{1 + t - 2\sqrt{t} \cos(\phi_q - \phi_l)} t^{\gamma-1} e^{in(\phi_q - \phi_l)} - \frac{1}{t} \left(\frac{1}{|t-1|} - \frac{1}{\sqrt{4t^2+1}} \right) \right] \tag{3.69}$$

with $t = q_{\perp}^2/l_{\perp}^2$. In arriving at Eq. (3.69) we have used Eqs. (A.13) and (A.15) from appendix section A.2 to do the angular integration of the second term in Eq. (3.67).

We see from Eq. (3.68) that $l_{\perp}^{2(\gamma-1)} e^{in\phi_l}$ is indeed an eigenfunction of the BFKL kernel K_{BFKL} , with $\chi(n, \gamma)$ the corresponding eigenvalue.

⁶ Our evaluation of the BFKL eigenvalue follows the strategy outlined in the review article by Del Duca (1995).

To perform the remaining angular integral in Eq. (3.69) we define a new complex variable $z = e^{i(\phi_q - \phi_l)}$ and write the integral as

$$\frac{i}{2\pi\sqrt{t}} \oint dz \frac{t^{\gamma-1} z^{|n|}}{(z - \sqrt{t})(z - \frac{1}{\sqrt{t}})}, \tag{3.70}$$

where the z -integral runs clockwise along a unit circle around the origin in the complex z -plane. To arrive at Eq. (3.70) we also noticed that the angular integral in Eq. (3.69) is an even function of n (and hence is a function of $|n|$), so that, to simplify the z -integration in Eq. (3.70), we can replace n by $|n|$. Performing the z -integral in Eq. (3.70) by the method of residues, we obtain for Eq. (3.69)

$$\chi(n, \gamma) = \int_0^\infty dt \left[\theta(1-t) \frac{t^{\gamma-1+|n|/2}}{1-t} + \theta(t-1) \frac{t^{\gamma-1-|n|/2}}{t-1} - \frac{1}{t} \left(\frac{1}{|t-1|} - \frac{1}{\sqrt{4t^2+1}} \right) \right]. \tag{3.71}$$

Employing the variable substitution $t \rightarrow 1/t$ for $t > 1$, we can rewrite Eq. (3.71) as

$$\chi(n, \gamma) = \int_0^1 dt \frac{t^{\gamma-1+|n|/2}}{1-t} + \int_0^1 dt \frac{t^{-\gamma+|n|/2}}{1-t} - 2 \int_0^1 \frac{dt}{1-t} - \int_0^1 \frac{dt}{t} + \int_0^\infty \frac{dt}{t\sqrt{4t^2+1}}. \tag{3.72}$$

Regulating the last two integrals in Eq. (3.72) by multiplying their integrands by t^ϵ , performing the integrations, and taking the limit $\epsilon \rightarrow 0$ one can see that they cancel each other. For the first three integrals in (3.72) we use the integral representation of the logarithmic derivative of the gamma function (see e.g. Gradshteyn and Ryzhik (1994), formula 8.361.7),

$$\psi(z) = \frac{d}{dz} \ln \Gamma(z) = \int_0^1 dt \frac{t^{z-1} - 1}{t-1} + \psi(1), \quad \text{Re } z > 0, \tag{3.73}$$

to write (Balitsky and Lipatov 1978)

$$\chi(n, \gamma) = 2\psi(1) - \psi\left(\gamma + \frac{|n|}{2}\right) - \psi\left(1 - \gamma + \frac{|n|}{2}\right). \tag{3.74}$$

Note that the sum of integrals in Eq. (3.72) gives a finite answer only for $0 < \text{Re } \gamma < 1$. Therefore, strictly speaking, the functions $l_\perp^{2(\gamma-1)} e^{in\phi_l}$ are the eigenfunctions of the BFKL kernel with eigenvalues $\chi(n, \gamma)$, (3.74), only for $0 < \text{Re } \gamma < 1$.

Expanding the general solution of the BFKL equation (3.58) over the eigenfunctions of the BFKL kernel and using the fact that the BFKL Green function is symmetric, $G(\vec{l}_\perp, \vec{l}'_\perp, Y) = G(\vec{l}'_\perp, \vec{l}_\perp, Y)$, which follows from its definition (see Fig. 3.5 and Eq. (3.26)), we write

$$G(\vec{l}_\perp, \vec{l}'_\perp, Y) = \sum_{n=-\infty}^\infty \int_{a-i\infty}^{a+i\infty} \frac{d\gamma}{2\pi i} C_{n,\gamma}(Y) l_\perp^{2(\gamma-1)} l'^2_{\perp}{}^{(\gamma^*-1)} e^{in(\phi-\phi')}, \tag{3.75}$$

where the $C_{n,\gamma}(Y)$ are some unknown functions, γ^* is the complex conjugate of γ , and ϕ and ϕ' are the angles between \vec{l}_\perp and \vec{l}'_\perp and some arbitrary axis in the transverse plane. The integral over γ runs along a contour which is a straight line parallel to the imaginary axis in the γ -plane, defined by $\text{Re } \gamma = a$ such that $0 < a < 1$.

Substituting Eq. (3.75) into Eq. (3.58) and using the eigenvalues from Eq. (3.74) we find

$$C_{n,\gamma}(Y) = C_{n,\gamma}^0 \exp \left\{ \frac{\alpha_s N_c}{\pi} \chi(n, \gamma) Y \right\}, \tag{3.76}$$

where the coefficient $C_{n,\gamma}^0$ is fixed by the initial condition (3.59):

$$C_{n,\gamma}^0 = \frac{1}{\pi}. \tag{3.77}$$

The initial condition (3.59) also fixes a as $1/2$. Using this along with Eqs. (3.76) and (3.77), in Eq. (3.75) we obtain the solution of the BFKL equation (3.58):

$$G(\vec{l}_\perp, \vec{l}'_\perp, Y) = \sum_{n=-\infty}^{\infty} \int_{1/2-i\infty}^{1/2+i\infty} \frac{d\gamma}{2\pi^2 i} \exp \left\{ \frac{\alpha_s N_c}{\pi} \chi(n, \gamma) Y \right\} l_\perp^{2(\gamma-1)} l_\perp'^{2(\gamma^*-1)} e^{in(\phi-\phi')}. \tag{3.78}$$

Since the integration contour in Eq. (3.78) runs along the $\text{Re } \gamma = 1/2$ line, if we define

$$\gamma = \frac{1}{2} + i\nu \tag{3.79}$$

with real ν we can rewrite Eq. (3.78) as

$$G(\vec{l}_\perp, \vec{l}'_\perp, Y) = \sum_{n=-\infty}^{\infty} \int_{-\infty}^{\infty} \frac{d\nu}{2\pi^2} \exp \left\{ \frac{\alpha_s N_c}{\pi} \chi(n, \nu) Y \right\} l_\perp^{-1+2i\nu} l_\perp'^{-1-2i\nu} e^{in(\phi-\phi')}, \tag{3.80}$$

where

$$\chi(n, \nu) = 2\psi(1) - \psi\left(\frac{1+|n|}{2} + i\nu\right) - \psi\left(\frac{1+|n|}{2} - i\nu\right). \tag{3.81}$$

Note that Eqs. (3.81) and (3.74) are related by the substitution (3.79).

Unfortunately an exact analytic evaluation of Eq. (3.80) does not appear to be feasible. We will therefore construct approximate solutions below.

Diffusion approximation Consider the case $l_\perp \sim l'_\perp$, i.e., the two transverse momentum scales involved in the problem are not very different from each other. To evaluate the ν -integral in Eq. (3.80) we will now employ the saddle point method, which we have already used in Sec. 2.4.6. A simple analysis of the saddle points of the function $\chi(n, \nu)$ at $\nu = 0$ allows one to conclude that at high energy, i.e., large rapidity Y , the dominant contribution to the amplitude is given by the $n = 0$ term in the sum in Eq. (3.80), as $\chi(n = 0, \nu = 0) >$

$\chi(n \neq 0, \nu = 0)$. We will therefore keep only the $n = 0$ term in Eq. (3.80) and write

$$G(\vec{l}_\perp, \vec{l}'_\perp, Y) \approx \int_{-\infty}^{\infty} \frac{d\nu}{2\pi^2 l_\perp l'_\perp} \exp\left\{ \bar{\alpha}_s \chi(0, \nu) Y + 2i\nu \ln \frac{l_\perp}{l'_\perp} \right\}; \tag{3.82}$$

here

$$\bar{\alpha}_s \equiv \frac{\alpha_s N_c}{\pi}. \tag{3.83}$$

Expanding $\chi(n = 0, \nu)$ around the saddle point at $\nu = 0$ we get

$$\chi(0, \nu) \approx 4 \ln 2 - 14\zeta(3)\nu^2, \tag{3.84}$$

where $\zeta(z)$ is the Riemann zeta function. Using Eq. (3.84) in Eq. (3.82) we perform the ν -integration, obtaining (Balitsky and Lipatov 1978)

$$G(\vec{l}_\perp, \vec{l}'_\perp, Y) \approx \frac{1}{2\pi^2 l_\perp l'_\perp} \sqrt{\frac{\pi}{14\zeta(3)\bar{\alpha}_s Y}} \exp\left\{ (\alpha_P - 1)Y - \frac{\ln^2(l_\perp/l'_\perp)}{14\zeta(3)\bar{\alpha}_s Y} \right\}, \tag{3.85}$$

where we have used, for the intercept of the perturbative BFKL pomeron,

$$\alpha_P - 1 = \frac{4\alpha_s N_c}{\pi} \ln 2. \tag{3.86}$$

The essential feature of Eq. (3.85) is that it shows that cross sections mediated by the BFKL ladder exchange grow as a power of the energy:

$$\sigma \sim e^{(\alpha_P - 1)Y} \sim s^{\alpha_P - 1}. \tag{3.87}$$

This behavior is reminiscent of pomeron exchange in pre-QCD language (see Eq. (3.20)). The BFKL ladder from Fig. 3.12 is therefore referred to as the “hard” (perturbative) pomeron or as the BFKL pomeron. We see that BFKL evolution modifies the energy-independent Low–Nussinov pomeron, which simply corresponds to a two-gluon exchange and has $\alpha_P - 1 = 0$, which makes the perturbative pomeron intercept $\alpha_P > 1$ as seen from Eq. (3.86). The numerical value of the BFKL intercept (3.86) is rather large: for $\alpha_s = 0.3$ one gets $\alpha_P - 1 \approx 0.79$, which is much larger than the “soft” pomeron intercept of 0.08 observed, say, for the total proton–proton scattering cross section (Donnachie and Landshoff 1992).

Double logarithmic approximation Let us consider the case $l_\perp \gg l'_\perp$. Now $\ln(l_\perp/l'_\perp)$ is large, and this may affect the location of the saddle point of the ν -integral in Eq. (3.80). The way the saddle point is shifted is shown in Fig. 3.14 for the $n = 0$ term in the series (3.80). As one can show analytically and as can be seen from Fig. 3.14, the effect of $(l_\perp/l'_\perp)^{2i\nu}$ in (3.80) is to shift the saddle point in the imaginary ν direction, moving it closer to the singularity of $\chi(0, \nu)$ at $\nu = i/2$. One can also show that the same is true for any integer n : the saddle point in the n th term in Eq. (3.80) is shifted toward the singularity of $\chi(n, \nu)$

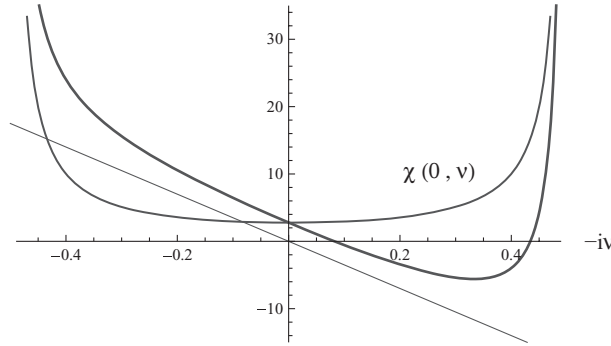


Fig. 3.14. The eigenvalue of the BFKL kernel $\chi(0, \nu)$ plotted as a function of $-i\nu$ (medium-bold line) for $\text{Re } \nu = 0$. The thin straight line is due to the linear term $2i\nu \ln(l_{\perp}/l'_{\perp})$ in the exponent of Eq. (3.82). The boldest curve is a sum of the medium-bold line and the thin straight line: it represents the complete expression in the exponent of Eq. (3.82). A color version of this figure is available online at www.cambridge.org/9780521112574.

at $\nu = i(|n| + 1)/2$. However, near these saddle points the n th term in the series (3.80) scales as

$$\frac{1}{l_{\perp}^2} \left(\frac{l'_{\perp}}{l_{\perp}} \right)^{|n|}; \tag{3.88}$$

we see that terms with $|n| > 0$ are suppressed by powers of $l'_{\perp}/l_{\perp} \ll 1$ compared with the $n = 0$ term (i.e., they are higher-twist corrections). Therefore the $n = 0$ term dominates again and, as before, we can work with Eq. (3.82).

Expanding the $n = 0$ eigenvalue of the BFKL kernel near $\nu = i/2$, we find that

$$\chi(0, \nu) \approx -\frac{i}{\nu - i/2}, \tag{3.89}$$

and the saddle point of the integral in Eq. (3.82) is then given by

$$\nu_{DLA} \approx \frac{i}{2} - i \sqrt{\frac{\bar{\alpha}_s Y}{\ln(l'_{\perp}/l_{\perp})}}. \tag{3.90}$$

Distorting the ν -integration contour to run through ν_{DLA} and expanding the exponent of Eq. (3.82) up to terms of order $(\nu - \nu_{DLA})^2$, we integrate the result over ν , obtaining

$$G(\vec{l}_{\perp}, \vec{l}'_{\perp}, Y) \approx \frac{1}{2\pi^{3/2} l_{\perp}^2} \frac{(\bar{\alpha}_s Y)^{1/4}}{\ln^{3/4}(l'_{\perp}/l_{\perp})} \exp \left\{ 2\sqrt{\bar{\alpha}_s Y \ln(l'_{\perp}/l_{\perp})} \right\}. \tag{3.91}$$

Comparing the exponential in Eq. (3.91) with that in Eq. (2.143) or, since here we are assuming a fixed coupling constant, with Eq. (2.159), we see that the DLA limit is indeed the same when obtained from the DGLAP or the BFKL equations! Identifying Y in Eq. (3.91) with $\ln 1/x$ in Eq. (2.159) and the transverse logarithm $\ln(l'_{\perp}/l_{\perp})$ in Eq. (3.91) with $\ln(Q^2/Q_0^2)$ in Eq. (2.159), we see complete agreement between the exponents in the two cases. The prefactor of Eq. (3.91) is different from what one would obtain in Eq. (2.159),

since here we are calculating a different quantity (the BFKL Green function) from the gluon distribution calculated in Chapter 2.

The agreement thus found between the DLA limits of BFKL and DGLAP is, of course, simply a self-consistency check: since the former resums powers of $\alpha_s \ln 1/x$ keeping the functions of transverse momentum exact while the latter resums powers of $\alpha_s \ln Q^2$ keeping functions of Bjorken x exact, they should include the same powers of $\alpha_s \ln 1/x \ln Q^2$. This result was illustrated in Table 3.1 in Section 3.1; we have proven it explicitly here.

We can also think of BFKL evolution as a property of the hadronic (or onium for the case at hand) light cone wave function, constructed similarly to the DGLAP evolution in the previous chapter. In essence one can absorb the shaded rectangle in Fig. 3.5, which includes the ladder in Fig. 3.12, into the light cone wave function of one onium. While we will demonstrate this explicitly in Chapter 4, here we absorb the BFKL evolution into the onium wave function by defining the *unintegrated gluon distribution* of an onium (cf. Eqs. (3.23) and (3.26)):

$$\begin{aligned} \phi(x_{Bj}, k_{\perp}^2) &= \frac{\alpha_s C_F}{\pi} \int d^2x_{\perp} \int_0^1 dz |\Psi(\vec{x}_{\perp}, z)|^2 \\ &\times \int \frac{d^2l_{\perp}}{l_{\perp}^2} (2 - e^{-i\vec{l}_{\perp} \cdot \vec{x}_{\perp}} - e^{i\vec{l}_{\perp} \cdot \vec{x}_{\perp}}) G(\vec{k}_{\perp}, \vec{l}_{\perp}, y = \ln 1/x_{Bj}). \end{aligned} \quad (3.92)$$

One can show that in the small- x LLA the unintegrated gluon distribution $\phi(x_{Bj}, k_{\perp}^2)$ is related to the gluon distribution function (2.66) by

$$\phi(x, Q^2) = \frac{\partial x G(x, Q^2)}{\partial Q^2}. \quad (3.93)$$

This implies that $\phi(x, k_{\perp}^2)$ counts the number of partons in a hadron at a given value of k_{\perp} (and a given value of Bjorken x), unlike xG , which counts the number of partons with $k_{\perp} \leq Q$. This provides a physical interpretation of $\phi(x, k_{\perp}^2)$ as the unintegrated gluon distribution.

Looking at Eq. (3.58), it is clear that the unintegrated gluon distribution $\phi(x_{Bj}, k_{\perp}^2)$ from Eq. (3.92) obeys the same BFKL evolution equation:

$$\frac{\partial \phi(x, k_{\perp}^2)}{\partial \ln(1/x)} = \frac{\alpha_s N_c}{\pi^2} \int \frac{d^2q_{\perp}}{(\vec{k}_{\perp} - \vec{q}_{\perp})^2} \left[\phi(x, q_{\perp}^2) - \frac{k_{\perp}^2}{2q_{\perp}^2} \phi(x, k_{\perp}^2) \right]. \quad (3.94)$$

By analogy with how we arrived at Eq. (3.78), for an unpolarized axially symmetric onium state we can write the solution of Eq. (3.94) as

$$\phi(x, k_{\perp}^2) = \int_{-\infty}^{\infty} \frac{dv}{2\pi} C_v \exp \left\{ \frac{\alpha_s N_c}{\pi} \chi(0, v) \ln \frac{1}{x} \right\} k_{\perp}^{-1+2iv} \Lambda^{-1-2iv}, \quad (3.95)$$

with Λ some typical transverse momentum scale characterizing the onium (e.g. the inverse size of the onium) and C_v an unknown function determined by the initial conditions at $x = x_0$.

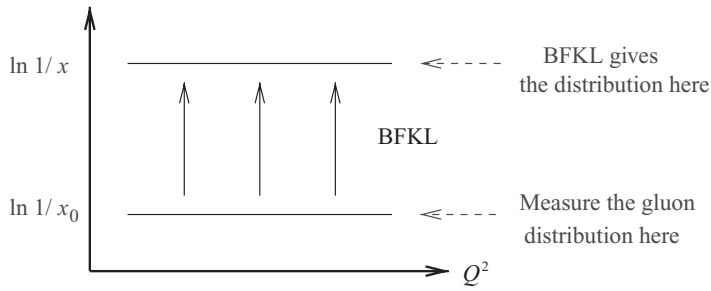


Fig. 3.15. The BFKL evolution in the $(\ln 1/x, Q^2)$ -plane. A color version of this figure is available online at www.cambridge.org/9780521112574.

The BFKL equation for the distribution function gives us the evolution in x . This is demonstrated in the $(\ln 1/x, Q^2)$ plane in Fig. 3.15. Given the initial unintegrated gluon distribution $\phi(x_0, k_\perp^2)$ one can find C_ν and then, substituting it into Eq. (3.95), one obtains an expression for the unintegrated gluon distribution $\phi(x, k_\perp^2)$ at other values of x (in the LLA approximation). Comparing Fig. 3.15 with Fig. 2.21 we can see the essential difference between the BFKL evolution in x and the DGLAP evolution in Q^2 .

If the transverse momentum of the gluons is not too large, i.e., $k_\perp \sim \Lambda$, while still much larger than Λ_{QCD} , we can evaluate the ν -integral in Eq. (3.95) in the diffusion approximation. Employing (3.84) and integrating yields an expression similar to Eq. (3.85):

$$\phi(x, k_\perp^2) \approx \frac{C_0}{2\pi} \frac{1}{k_\perp \Lambda} \sqrt{\frac{\pi}{14\zeta(3)\bar{\alpha}_s \ln(1/x)}} \left(\frac{1}{x}\right)^{\alpha_p-1} \exp\left\{-\frac{\ln^2(k_\perp/\Lambda)}{14\zeta(3)\bar{\alpha}_s \ln(1/x)}\right\}. \tag{3.96}$$

We see that the unintegrated gluon distribution (and therefore, owing to (3.93), the regular gluon distribution xG as well) generated by the BFKL evolution grows as a power of $1/x$ at small x :

$$\phi(x, k_\perp^2) \sim \left(\frac{1}{x}\right)^{\alpha_p-1}, \tag{3.97}$$

with $\alpha_p - 1$ given by Eq. (3.86). This should be contrasted with the growth of the gluon distribution at small x resulting from DGLAP evolution, as shown in Eq. (3.3). The small- x growth of a gluon distribution given by BFKL evolution is much faster than that given by the DGLAP equation.

Since BFKL evolution does not impose any transverse momentum ordering, the partons generated by the evolution (3.94) have comparable transverse momenta, as given by Eq. (3.60b), and, according to Eq. (3.61), they are ordered in x ,

$$x_1 \ll x_2 \ll \dots \ll x_n \ll 1, \tag{3.98}$$

since $y = \ln(P^-/k^-) = \ln 1/x$ for the onium moving in the light cone minus direction.

It is instructive to consider the spatial distribution of the partons generated by BFKL evolution. Since the typical transverse size (wavelength) of a parton is $x_\perp \approx 1/k_\perp$, we see

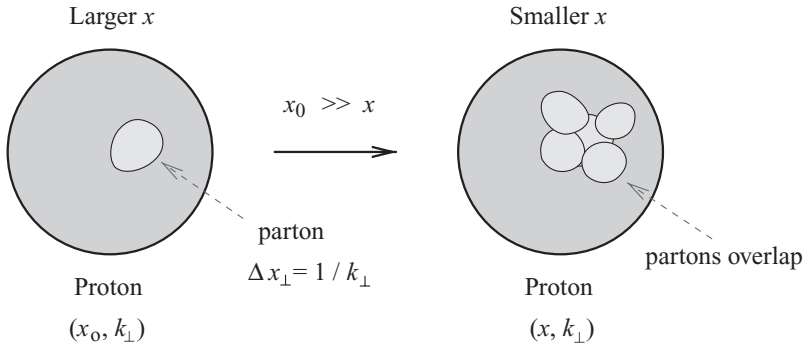


Fig. 3.16. Transverse coordinate space representation of BFKL evolution. The blobs indicate gluons. (Reprinted from Jalilian-Marian and Kovchegov (2006), with permission from Elsevier.) A color version of this figure is available online at www.cambridge.org/9780521112574.

that Eq. (3.60b) implies that

$$x_{1\perp} \sim x_{2\perp} \sim \dots \sim x_{n\perp}, \quad (3.99)$$

that is, BFKL evolution in, say, a proton wave function generates partons of roughly the same transverse size. At the same time, owing to Eq. (2.56) the ordering in Bjorken x simply indicates that gluons with smaller x have a larger typical longitudinal spread. The BFKL evolution in transverse coordinate space is shown in Fig. 3.16. As Bjorken x decreases, more gluons are generated in the hadron wave function. The partons (gluons) produced are of roughly the same transverse size. (Compare this with the DGLAP evolution in Fig. 2.22.) As a result, after a sufficient number of gluons is generated they may start to overlap with each other in transverse space, as shown in the right-hand panel of Fig. 3.16. This leads to the creation of regions of high parton density in the hadronic wave functions. Therefore one can think of the BFKL equation as a “high parton density machine”: it results in high parton density in the hadronic wave functions. This is what makes BFKL (and small- x physics in general) interesting, but it also leads to some problems for BFKL evolution, which we will discuss below.

3.3.5 Bootstrap property of the BFKL equation*

Let us now explain the reggeization of a t -channel gluon in the BFKL ladder. There is a widespread belief in the community that gluon reggeization may be a fundamental property of high energy QCD: thus, while gluon reggeization is not important for the material we present below, no book on high energy QCD would be complete without the presentation of this remarkable feature of strong interactions.

In Sec. 3.3.2 we found the lowest-order correction to the one-gluon exchange amplitude in Fig. 3.3. This correction turned out to be rather simple and is given by Eqs. (3.51) and (3.52). To incorporate the higher-order leading- $\ln s$ corrections into the t -channel gluon

propagator, we will again use the dispersion relation (3.43): it follows from Eq. (3.43) that to construct the full amplitude we need to know only the imaginary part of the amplitude. As in the calculation in Sec. 3.3.2, we will need the diagrams with color-octet exchanges in the t -channel that have an imaginary part. Diagrams F and G in Fig. 3.9 are the lowest-order examples of such graphs, for s - and u -channel processes respectively. We now need to find the leading- $\ln s$ corrections to the imaginary part of diagram F (diagram G can be obtained by replacing s by u in diagram F, as we have pointed out before). There are two important differences between the imaginary part of diagram F in Fig. 3.9 and the diagram in Fig. 3.4, for which the leading logarithmic corrections were summed by the BFKL evolution equation. (i) As can be seen from Eq. (3.50), the color structure of the leading high energy part of diagram F is the same as for the single-gluon exchange amplitude (3.17), which implies that at high energy the two t -channel gluons in diagram F are in the color-octet state. This is to be contrasted with the diagram in Fig. 3.4, which is a diagram for the total cross section; therefore, the two t -channel gluons in it are in the color-singlet state. (ii) Since the diagram in Fig. 3.4 is for the total cross section, there is no net momentum transfer between the onium states in the corresponding forward amplitude. At the same time, in diagram F there is no restriction on the momentum transfer, which is in general nonzero.

One may argue (see Fadin, Kuraev, and Lipatov (1976)) that, despite the two differences stated above, the leading- $\ln s$ corrections to diagram F can still be resummed using the BFKL-like ladder from Fig. 3.12. Items (i) and (ii) above simply require that now the ladder should be nonforward, with the t -channel state projected on the color-octet configuration. We start by rewriting the imaginary part of the color-octet t -channel-exchange $qq \rightarrow qq$ amplitude $M_{qq \rightarrow qq}^{(8)}$ as (cf. Eq. (3.46))

$$\text{Im } M_{qq \rightarrow qq}^{(8)}(\vec{q}_\perp) = 4\alpha_s^2 (t^b t^a)_{i'i} (t^b t^a)_{j'j} \delta_{\sigma_1 \sigma_1'} \delta_{\sigma_2 \sigma_2'} s \times \int \frac{d^2 l_\perp}{l_\perp^2 (\vec{l}_\perp - \vec{q}_\perp)^2} \frac{d^2 l''_\perp}{l''_\perp{}^2 (\vec{l}''_\perp - \vec{q}_\perp)^2} G^{(8)}(\vec{l}_\perp, \vec{l}''_\perp; \vec{q}_\perp; Y), \quad (3.100)$$

where $G^{(8)}(\vec{l}_\perp, \vec{l}''_\perp; \vec{q}_\perp; Y)$ is the color-octet nonforward analogue of the BFKL Green function defined in Eq. (3.26) above. The octet nonforward Green function $G^{(8)}$ is illustrated on the left-hand side of Fig. 3.17. Equation (3.46) representing diagram F in Fig. 3.9 is recovered by inserting

$$G^{(8)}(\vec{l}_\perp, \vec{l}''_\perp; \vec{q}_\perp; Y = 0) = l_\perp''^2 (\vec{l}_\perp'' - \vec{q}_\perp)^2 \delta^2(\vec{l}_\perp - \vec{l}''_\perp) \quad (3.101)$$

into Eq. (3.100).

By analogy with the construction of the BFKL equation we can construct the evolution equation for the octet Green function, following the prescription indicated in Fig. 3.17. First we note that the virtual corrections in the color-octet case are the same as they were in the color-singlet case of BFKL evolution, given by Eq. (3.55). The real emission in the case of BFKL evolution was obtained by squaring the Lipatov vertex (3.36); however, since now the process is nonforward, the t -channel gluons' momenta should be different in the two

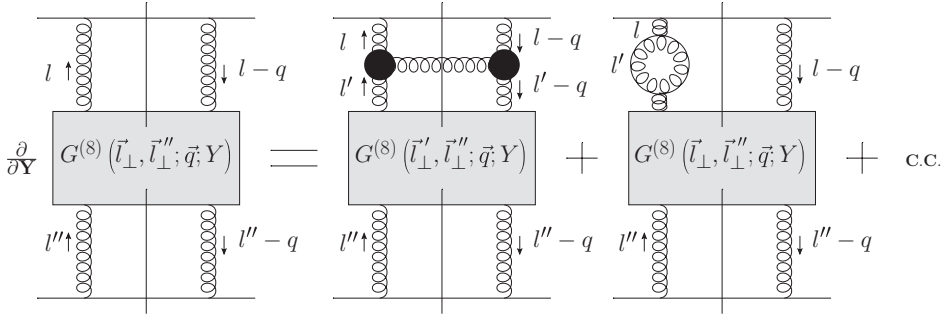


Fig. 3.17. Diagrammatic representation of the leading- $\ln s$ evolution of the color-octet nonforward Green function. The notation is the same as in Fig. 3.11.

factors of the Lipatov vertex. In the end we obtain the following evolution equation:

$$\begin{aligned} \frac{\partial}{\partial Y} G^{(8)}(\vec{l}_\perp, \vec{l}'_\perp; \vec{q}_\perp; Y) &= \int d^2 l'_\perp K_{NF}^{(8)}(\vec{l}_\perp, \vec{l}'_\perp; \vec{q}_\perp) G^{(8)}(\vec{l}'_\perp, \vec{l}''_\perp; \vec{q}_\perp; Y) \\ &+ \omega_G(l_\perp) G^{(8)}(\vec{l}_\perp, \vec{l}'_\perp; \vec{q}_\perp; Y) \\ &+ \omega_G(|\vec{l}_\perp - \vec{q}_\perp|) G^{(8)}(\vec{l}_\perp, \vec{l}''_\perp; \vec{q}_\perp; Y). \end{aligned} \tag{3.102}$$

The terms containing $\omega_G(l_\perp)$, which is defined in Eq. (3.52), are due to virtual corrections. The part of the nonforward color-octet BFKL kernel coming from real-gluon emission,

$$K_{NF}^{(8)}(\vec{l}_\perp, \vec{l}'_\perp; \vec{q}_\perp) = \frac{\alpha_s N_c}{4\pi^2} \left[\frac{l_\perp^2}{l_\perp'^2 (\vec{l}_\perp - \vec{l}'_\perp)^2} + \frac{(\vec{l}_\perp - \vec{q}_\perp)^2}{(\vec{l}'_\perp - \vec{q}_\perp)^2 (\vec{l}_\perp - \vec{l}'_\perp)^2} - \frac{q_\perp^2}{l_\perp'^2 (\vec{l}'_\perp - \vec{q}_\perp)^2} \right], \tag{3.103}$$

results from the (nonforward) square of the Lipatov vertex (3.36) divided by the propagators of the two t -channel gluons below the vertex (the l' - and $(l' - q)$ -lines in the first diagram on the right-hand side of Fig. 3.17). In arriving at Eq. (3.102) we have also employed the fact that, for the color-octet two-gluon state in the t -channel, the color factor generated by the real part of the kernel is equal to $N_c/2$ instead of N_c , which one has for the color-singlet (BFKL) evolution. The initial condition for Eq. (3.102) is given by Eq. (3.101).

While the nonforward ($t \neq 0$) BFKL equation (3.102) appears to be more complicated than the forward ($t = 0$) BFKL equation (3.58), in fact its solution is rather straightforward if one is just interested in the resulting scattering amplitude. We begin by defining

$$\bar{G}^{(8)}(\vec{l}_\perp; \vec{q}_\perp; Y) \equiv \int \frac{d^2 l''_\perp}{l''_\perp{}^2 (\vec{l}''_\perp - \vec{q}_\perp)^2} G^{(8)}(\vec{l}_\perp, \vec{l}''_\perp; \vec{q}_\perp; Y). \tag{3.104}$$

For this new quantity the evolution equation is the same as (3.102):

$$\begin{aligned} \frac{\partial}{\partial Y} \bar{G}^{(8)}(\vec{l}_\perp; \vec{q}_\perp; Y) &= \int d^2 l'_\perp K_{NF}^{(8)}(\vec{l}_\perp, \vec{l}'_\perp; \vec{q}_\perp) \bar{G}^{(8)}(\vec{l}'_\perp; \vec{q}_\perp; Y) \\ &\quad + \omega_G(l_\perp) \bar{G}^{(8)}(\vec{l}_\perp; \vec{q}_\perp; Y) + \omega_G(|\vec{l}_\perp - \vec{q}_\perp|) \bar{G}^{(8)}(\vec{l}_\perp; \vec{q}_\perp; Y) \end{aligned} \tag{3.105}$$

with initial condition $\bar{G}^{(8)}(\vec{l}_\perp; \vec{q}_\perp; Y = 0) = 1$ (cf. Eq. (3.101)). Now we write $\bar{G}^{(8)}$ as an inverse Laplace transform,

$$\bar{G}^{(8)}(\vec{l}_\perp; \vec{q}_\perp; Y) = \int \frac{d\omega}{2\pi i} e^{\omega Y} \bar{G}_\omega^{(8)}(\vec{l}_\perp; \vec{q}_\perp), \tag{3.106}$$

where, as usual, the ω -integration runs parallel to the imaginary axis in the complex ω -plane to the right of all the singularities of the integrand. Substituting (3.106) into Eq. (3.105) and performing a Laplace transform on both sides of the resulting equation yields the *bootstrap equation*

$$\begin{aligned} &[\omega - \omega_G(l_\perp) - \omega_G(|\vec{l}_\perp - \vec{q}_\perp|)] \bar{G}_\omega^{(8)}(\vec{l}_\perp; \vec{q}_\perp) \\ &= 1 + \int d^2 l'_\perp K_{NF}^{(8)}(\vec{l}_\perp, \vec{l}'_\perp; \vec{q}_\perp) \bar{G}_\omega^{(8)}(\vec{l}'_\perp; \vec{q}_\perp). \end{aligned} \tag{3.107}$$

(We have also made use of the initial condition $\bar{G}^{(8)}(\vec{l}_\perp; \vec{q}_\perp; Y = 0) = 1$.) It is easy to see that

$$\bar{G}_\omega^{(8)}(\vec{l}_\perp; \vec{q}_\perp) = \frac{1}{\omega - \omega_G(q_\perp)} \tag{3.108}$$

in fact solves Eq. (3.107) for the kernel given by Eq. (3.103). Substituting Eq. (3.108) into Eq. (3.106) we obtain the solution of Eq. (3.105):

$$\bar{G}^{(8)}(\vec{l}_\perp; \vec{q}_\perp; Y) = e^{\omega_G(q_\perp)Y}. \tag{3.109}$$

Using Eqs. (3.109) and (3.104) in Eq. (3.100) we obtain the imaginary part of the color-octet exchange amplitude,

$$\text{Im}M_{qq \rightarrow qq}^{(8)}(\vec{q}_\perp) = 4\alpha_s^2 (t^b t^a)_{i'i} (t^b t^a)_{j'j} \delta_{\sigma_1 \sigma'_1} \delta_{\sigma_2 \sigma'_2} s \int \frac{d^2 l_\perp}{l_\perp^2 (|\vec{l}_\perp - \vec{q}_\perp|^2)} e^{\omega_G(q_\perp)Y}, \tag{3.110}$$

where, as usual in the leading- $\ln s$ approximation, we have $Y = \ln(s/m_\perp^2)$ with m_\perp some transverse momentum scale, the exact value of which is outside the precision of the approximation.

To obtain the complete color-octet exchange amplitude we substitute Eq. (3.110) into Eq. (3.43) (adding the u -channel contribution obtained from Eq. (3.110) on replacing s by u). Integrating in the leading-logarithmic approximation, we obtain the high energy color-octet exchange amplitude

$$M_{qq \rightarrow qq}^{(8)}(\vec{q}_\perp) = M_{qq \rightarrow qq}^0(\vec{q}_\perp) e^{\omega_G(q_\perp)Y}, \tag{3.111}$$

where M^0 is the single-gluon exchange amplitude given in Eq. (3.17). Note that Eq. (3.111) is in effect the same as Eq. (3.53), which we employed in deriving the BFKL evolution equation.

Equation (3.107) represents the so-called “bootstrap” idea, which states that the evolution of the reggeized gluon is given by the evolution of the color-octet t -channel state of two gluons. It is referred to as the *bootstrap equation*. It has been conjectured that the bootstrap equation (3.107) with its rather simple solution (3.108) holds at any order in α_s . (Indeed both $K_{NF}^{(8)}$ and ω_G receive corrections at higher orders in α_s : the conjecture states that these corrections leave Eqs. (3.107) and (3.108) in exactly the same form as shown above, only modifying $K_{NF}^{(8)}$ and ω_G in them.) So far the conjecture has been verified at the two lowest orders in α_s : the leading order- α_s result is presented here, and the validity of the bootstrap equation at order α_s^2 has been shown by Fadin, Kotsky, and Fiore (1995, 1996).

We see that the bootstrap equation (3.107) with its solution leading to Eq. (3.111) implies that the nonforward BFKL equation for the color-octet state of two gluons should lead to a reggeized gluon with the Regge trajectory $\alpha_G(q_\perp) = 1 + \omega_G(q_\perp)$. This observation completes the proof that in high energy scattering a t -channel gluon should be treated as a reggeized gluon whose spin depends on its transverse momentum.

3.3.6 Problems of BFKL evolution: unitarity and diffusion

The BFKL equation represents an important step towards understanding the high energy asymptotics of QCD. Nonetheless, as for every major scientific advance, the BFKL equation raises some important questions, which we will describe in this section. In particular we will show that as the collision energy increases (i) the leading-logarithmic BFKL equation violates unitarity and (ii) the transverse momenta of the gluons inside the BFKL ladder tend to drift to both the UV and IR, the latter drift eventually leading to a violation of the assumption of the perturbative nature of the interactions.

The Froissart–Martin bound

We begin our presentation of the unitarity bound with a discussion of the black disk limit. Imagine the high energy scattering of a point particle on a “black disk” of radius R . Using the language of nonrelativistic quantum mechanics one can think of the black disk as an infinite potential well occupying a spherical region of space. It can then be shown that the total cross section for the scattering of the point particle from the disk is limited from above by

$$\sigma_{tot} \leq 2\pi R^2 \quad (3.112)$$

(see Landau and Lifshitz (1958), vol. 3, Chapter 131, and the discussion in Appendix B). The total cross section can be as large as twice the geometric cross sectional area of the disk: this doubling is due to Babinet’s principle in optics, which states that the diffractive patterns of complementary screens are identical (see Jackson (1998) or Landau and Lifshitz (1958), vol. 2, Chapter 61). In optics Babinet’s principle implies that the amount of light

diffracted by a screen is equal to the amount of light it absorbs. For very high energy scattering it implies that, when the scattering occurs from a black disk, the elastic (σ_{el}) and inelastic (σ_{inel}) cross sections are equal. Since the inelastic cross section is equal to the cross sectional area of the disk πR^2 , we have $\sigma_{el} = \sigma_{inel} = \pi R^2$, so that the total cross section is $\sigma_{tot} = \sigma_{inel} + \sigma_{el} = 2\pi R^2$.

Our derivation of the Froissart–Martin bound will incorporate the argument put forward by Heisenberg (1952, 1939) with the proof devised by Froissart (1961) and Martin (1969). Consider hadron–hadron scattering at impact parameter b . Let us assume that b is large enough that the black-disk limit described above has not been reached. Inspired by the above examples of the BFKL equation and the Low–Nussinov pomeron, we may assume that the interaction between the hadrons is accomplished though an exchange of one or several particles, so that the cross section grows as some positive power Δ of the energy: $\sigma \sim s^\Delta$. At the same time the strength of the interaction should fall off as we increase b : the slowest physically possible fall off is the exponential $e^{-2m_\pi b}$, where m_π is the mass of the lightest QCD bound state, the pion.⁷ (As the pion has negative parity, the exchange of a single pion cannot contribute to the total cross section, hence we need to exchange two pions, one in the amplitude and the other in the complex-conjugate amplitude.) We thus have a probability p of interaction that scales with energy and impact parameter as follows:

$$p \sim s^\Delta e^{-2m_\pi b}. \tag{3.113}$$

The interaction gets strong when the probability is of order 1. In fact, for p of order 1 the black-disk-limit behavior should begin to set in. Thus the upper limit on the radius of the black disk can be determined by requiring that $p \approx 1$, which, as we can see from Eq. (3.113), occurs at impact parameter b^* defined by

$$s^\Delta e^{-2m_\pi b^*} = 1, \tag{3.114}$$

which gives

$$R = b^* \sim \frac{\Delta}{2m_\pi} \ln s. \tag{3.115}$$

Since b^* is the upper bound on the black-disk radius, the total cross section, dominated by the black-disk contribution, is then limited by $2\pi R^2 = 2\pi b^{*2}$, yielding eventually

$$\sigma_{tot} \leq \frac{\pi \Delta^2}{2m_\pi^2} \ln^2 s. \tag{3.116}$$

We conclude that the total cross section in QCD cannot grow faster than the logarithm of energy squared. Equation (3.116) is known as the *Froissart–Martin bound* and was first rigorously proven by Froissart (1961) and Martin (1969) (see also Lukaszuk and Martin (1967)).

⁷ As discussed by Nussinov (2008), it is possible that for realistic estimates the pion mass in this exponential should in fact be replaced by the mass of the lightest glueball (a QCD bound state having no valence quarks) since, as we have seen above, gluons dominate in high energy interactions.

As we saw above (see e.g. Eq. (3.87)), the BFKL equation in the diffusion approximation implies that the total cross section grows as a power of the energy,

$$\sigma_{tot}^{BFKL} \sim s^{\alpha_p - 1}, \quad (3.117)$$

which clearly violates the Froissart–Martin bound (3.116). Things do not get much better in the double logarithmic limit of the BFKL equation, which, according to Eq. (3.91), gives

$$\sigma_{tot}^{DLA\ BFKL} \sim \exp \left\{ 2\sqrt{\bar{\alpha}_s \ln s \ln(l_\perp^2/l_\perp'^2)} \right\}, \quad (3.118)$$

where l_\perp and l'_\perp are the momentum scales at the two ends of the BFKL ladder, with $l_\perp \gg l'_\perp$ in the DLA. The energy growth of the cross section in Eq. (3.118) is exponential in $\sqrt{\ln s}$, and, as such, is much faster than any power of $\ln s$: therefore, DLA BFKL also violates the Froissart–Martin bound. Note that since DLA BFKL is equivalent to DLA DGLAP, the DGLAP evolution also violates unitarity, making this an inherent problem of standard perturbative QCD: no matter how high the larger perturbative scale l_\perp is, at sufficiently high energy s , unitarity will still be violated, as follows from Eq. (3.118). We thus conclude that unitarity violation happens at perturbatively large momentum scales, where perturbative QCD is still applicable. Thus, it is natural to expect that the resolution of this problem should also happen through a QCD perturbative mechanism. We will discuss shortly how a nonlinear evolution equation was proposed by Gribov, Levin, and Ryskin (GLR) to remedy this problem of the BFKL evolution (Gribov, Levin, and Ryskin 1983).

One may indeed argue that in deriving the Froissart–Martin bound above we have used the fact that QCD is a confining theory with bound states such as pions, which one certainly does not see in the perturbative calculations leading to the BFKL equation. Therefore, since the QCD mass gap m_π is not present in perturbation theory (which has a zero mass gap), one should not expect BFKL evolution to satisfy the Froissart–Martin bound. This argument is indeed correct; however, as we will show below, the BFKL equation can also be written in impact parameter space. As we argue in Appendix B, in impact parameter space the high energy cross sections are given by

$$\sigma_{tot} = 2 \int d^2b \left[1 - \text{Re } S(s, \vec{b}_\perp) \right], \quad (3.119a)$$

$$\sigma_{el} = \int d^2b \left| 1 - S(s, \vec{b}_\perp) \right|^2, \quad (3.119b)$$

$$\sigma_{inel} = \int d^2b \left[1 - |S(s, \vec{b}_\perp)|^2 \right], \quad (3.119c)$$

with $S(s, \vec{b}_\perp)$ the forward matrix element of the scattering S -matrix. Since at high energy $S \rightarrow 0$ we see that $d\sigma_{tot}/d^2b_\perp \leq 2$, which is equivalent to the black-disk limit (3.112). The BFKL-dominated total cross section at a fixed impact parameter b grows as a power of the energy s , eventually violating the bound $d\sigma_{tot}/d^2b_\perp \leq 2$ at very high energy. Thus the BFKL equation violates unitarity not only through the fast growth of the black-disk radius but also by the fact that the cross section at each impact parameter becomes larger than the black-disk bound $d\sigma_{tot}/d^2b_\perp \leq 2$. While the former problem cannot be remedied in QCD

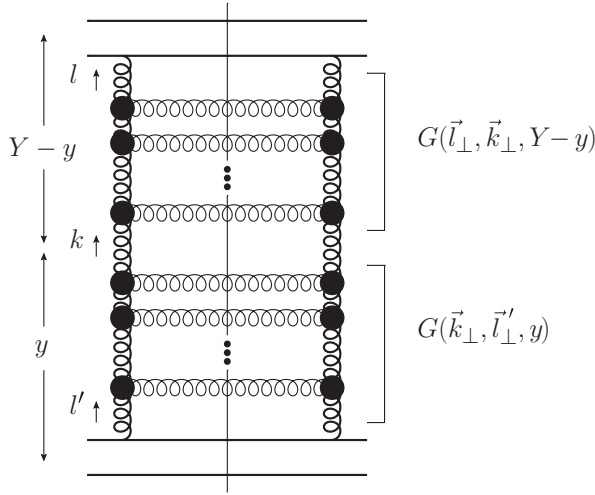


Fig. 3.18. The BFKL ladder, with a t -channel gluon with momentum \vec{k}_\perp singled out for study of its momentum distribution. The vertical solid line denotes a cut.

perturbation theory, one may hope to remedy the latter problem; as we will see below it is cured by the use of nonlinear evolution equations.

We conclude that the BFKL equation violates unitarity (or, more precisely, the black-disk limit). Therefore one would expect it to be modified at very high energies, in order to satisfy those bounds. This is the first problem of BFKL evolution.

Diffusion into the infrared

The second problem of BFKL evolution becomes apparent if we look “inside” the BFKL ladder. To do this, let us pick a particular gluon in the ladder sufficiently far from the ends of the ladder. This is illustrated in Fig. 3.18, where we are considering the transverse momentum distribution of a t -channel gluon with momentum \vec{k}_\perp and rapidity y (of adjacent rungs) inside the BFKL ladder. The ladder can be split into two sub-ladders, each of which is a BFKL ladder in its own right, as indicated by the right-hand square brackets in Fig. 3.18. The BFKL Green function (3.80) can correspondingly be written as a convolution of two BFKL Green functions,

$$G(\vec{l}_\perp, \vec{l}'_\perp, Y) = \int d^2k_\perp G(\vec{l}_\perp, \vec{k}_\perp, Y - y) G(\vec{k}_\perp, \vec{l}'_\perp, y), \quad (3.120)$$

where the net rapidity interval is Y and the transverse momenta at the ends of the original ladder are \vec{l}_\perp and \vec{l}'_\perp .

Let us assume that all the transverse momenta involved are comparable, $l_\perp \sim l'_\perp \sim k_\perp$, so that we can use the diffusion approximation (3.85). As follows from Eq. (3.120), the k_\perp -distribution dn/d^2k_\perp for the t -channel gluon in Fig. 3.18 is given by the product of the

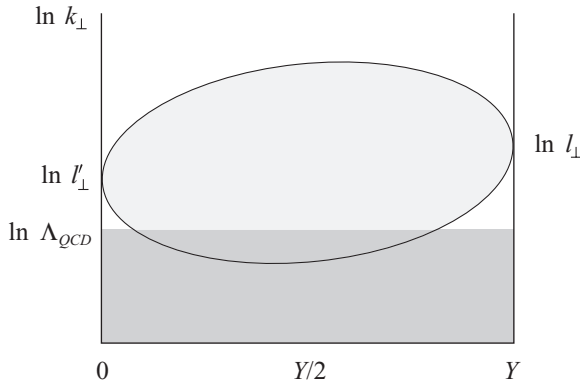


Fig. 3.19. The $\ln k_{\perp}$ -distribution of the momentum of a t -channel gluon inside the BFKL ladder (shaded oval). For a large enough rapidity interval Y the $\ln k_{\perp}$ -distribution overlaps with the nonperturbative region $k_{\perp} \lesssim \Lambda_{QCD}$ (the shaded rectangle). A color version of this figure is available online at www.cambridge.org/9780521112574.

two BFKL Green functions and, in the diffusion approximation (3.85), it is proportional to

$$\begin{aligned} \frac{dn}{d \ln k_{\perp}^2} &= k_{\perp}^2 G(\vec{l}_{\perp}, \vec{k}_{\perp}, Y - y) G(\vec{k}_{\perp}, \vec{l}'_{\perp}, y) \\ &\sim \exp \left\{ -\frac{\ln^2(l_{\perp}/k_{\perp})}{14\zeta(3)\bar{\alpha}_s(Y - y)} - \frac{\ln^2(k_{\perp}/l'_{\perp})}{14\zeta(3)\bar{\alpha}_s y} \right\}. \end{aligned} \tag{3.121}$$

We see that the distribution in $\ln k_{\perp}^2$ is Gaussian. The width of the distribution depends on the rapidity, reaching a maximum at $y = Y/2$. As we increase the total energy (or, equivalently, the net rapidity interval Y), the $\ln k_{\perp}^2$ -distribution at $y \approx Y/2$ gets broader: the values of k_{\perp} deviate more and more from the original momenta l_{\perp} and l'_{\perp} at the ends of the ladder. This feature of BFKL evolution is potentially dangerous in QCD, for the following reason. Suppose that to justify the use of perturbative QCD we choose $l_{\perp} \sim l'_{\perp} \gg \Lambda_{QCD}$. As we increase the net rapidity interval Y the transverse momentum in the ladder diffuses away from $l_{\perp} \sim l'_{\perp}$, fluctuating both into the UV and IR, so that at $y = Y/2$ we have

$$l_{\perp} e^{-\text{const} \times \sqrt{Y/2}} \lesssim k_{\perp} \lesssim l_{\perp} e^{\text{const} \times \sqrt{Y/2}}. \tag{3.122}$$

(We have assumed for simplicity that $l_{\perp} = l'_{\perp}$ and that $\text{const} = \sqrt{(7/2)\zeta(3)\bar{\alpha}_s}$ in Eq. (3.122).) Clearly, for large enough energies or rapidities Y , the lower limit of the k_{\perp} -range in Eq. (3.122) may reach Λ_{QCD} , invalidating the applicability of perturbative QCD to the problem (Bartels 1993b, Bartels, Lotter, and Vogt 1996). The $\ln k_{\perp}^2$ -distribution is plotted in Fig. 3.19; owing to its cigar-like shape, it is sometimes referred to as the *Bartels cigar* (Bartels 1993b).

The problem of BFKL evolution becoming nonperturbative at high Y values implies that we cannot use the BFKL equation at arbitrarily high energies: its applicability is thus limited. Therefore, either the true high energy asymptotics of QCD is nonperturbative and

cannot be described by perturbative QCD or it may still be perturbative and described by a different evolution equation that does not have the same IR problem as the BFKL equation. We will show in the next chapter that the latter option is in fact the case.

3.4 The nonlinear Gribov–Levin–Ryskin and Mueller–Qiu evolution equation

3.4.1 The physical picture of parton saturation

In order to understand how the BFKL unitarity problem can be addressed, let us first determine the kinematic region where unitarity is violated by BFKL evolution. Consider onium–onium scattering mediated by the BFKL ladder exchange studied above. The expression for the total onium–onium scattering cross section can be obtained by substituting the LLA Green function (3.85) into Eq. (3.26). At the moment we are not interested in the exact result (see Exercise 3.5 at the end of the chapter) and will only note that in Eq. (3.26) the typical momenta are $l_{\perp} \approx 1/x_{1\perp}$ and $l'_{\perp} \approx 1/x_{2\perp}$. The total cross section is then

$$\sigma_{tot}^{onium+onium} \sim \alpha_s^2 x_{1\perp} x_{2\perp} e^{(\alpha_P-1)Y}, \tag{3.123}$$

where we have kept only the most physically important factors, those depending on the total rapidity Y and on the sizes of the onia. We know, however, that the cross section should be bounded from above by the black-disk limit, $\sigma_{tot}^{onium+onium} \leq 2\pi R^2$. While the radius of the black disk R grows logarithmically with energy, as shown in Eq. (3.115), for the moment we will forget about this growth since it is much slower than the power-of-energy growth of the total cross section in Eq. (3.123), and will fix R to be of the order of a typical hadronic radius, $R \approx r_h$. In fact let us assume that our onium–onium scattering models a DIS event, in which the first onium comes from the decay of a virtual photon and the other mimics the proton (we will present this dipole picture of DIS in more detail in the next chapter). Then $x_{2\perp} \approx r_h$ and $x_{1\perp} \approx 1/Q$, with Q the virtuality of the photon (the only scale at the photon end of the ladder). Imposing the black-disk limit on Eq. (3.123) yields

$$\alpha_s^2 \frac{r_h}{Q} e^{(\alpha_P-1)Y} \leq 2\pi r_h^2. \tag{3.124}$$

The equality is reached at the *saturation scale* $Q = Q_s$ given by

$$Q_s \sim \alpha_s^2 \Lambda_{QCD} e^{(\alpha_P-1)Y} = \alpha_s^2 \Lambda_{QCD} \left(\frac{1}{x}\right)^{\alpha_P-1}, \tag{3.125}$$

where, for simplicity, we have replaced the typical hadronic size r_h with $1/\Lambda_{QCD}$: the two scales differ only by a constant coefficient, irrelevant for our rough estimates. The saturation momentum Q_s is a new dimensional scale in the problem (Gribov, Levin, and Ryskin 1983, Mueller and Qiu 1986, McLerran and Venugopalan 1994a).

We conclude that a violation of unitarity occurs for $Q < Q_s$. Note that for very small Bjorken x (large Y) the saturation scale can be much larger than the confinement scale, $Q_s \gg \Lambda_{QCD}$. This implies that the violation of unitarity starts at short distances of the

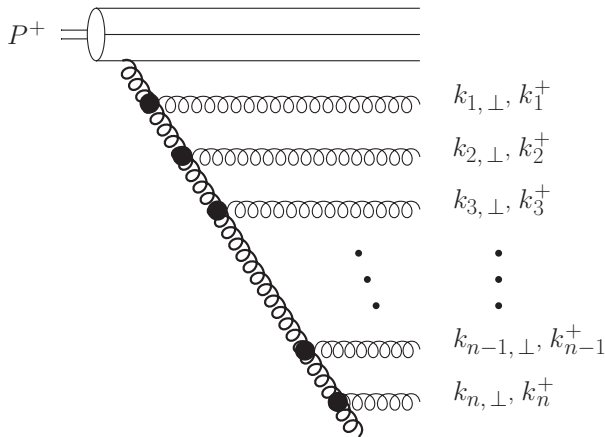


Fig. 3.20. The BFKL evolution of Fig. 3.13 shown here as a time-ordered gluon cascade in the proton wave function, in the IMF/Bjorken or Breit frames.

order of $1/Q_s$, still in the domain of validity of perturbative QCD. Therefore, the unitarity problem of BFKL evolution has to be solved in the framework of perturbative QCD.

To address this unitarity problem we first need to understand what goes wrong with BFKL evolution. This is easier to do if we absorb the BFKL ladder into the wave function of a hadron in DIS in the Breit frame, as for the DGLAP evolution in the previous chapter. (Formally, the BFKL light cone wave function is constructed in the next chapter.) The small- x evolution then appears as a cascade in the proton’s wave function, shown in Fig. 3.20 (compare with Figs. 2.25 and 2.10). The fast proton will decay into a system of partons long before the interaction with the virtual photon, which is at rest. The time ordering of emissions is given by Eq. (2.156) in the DLA DGLAP case (the proton is moving in the light cone plus direction)

$$x_1^+ \gg x_2^+ \gg \dots \gg x_n^+, \tag{3.126}$$

and this would still be valid: in the general BFKL case the DGLAP ordering of transverse momenta (2.149) is replaced by the comparability of all transverse momenta, as given by Eq. (3.60b), with the ordering (2.150) of longitudinal momenta from DLA DGLAP still in place (see Eq. (3.60a)). The latter fact insures that the typical lifetimes of gluon fluctuations, given by $x_i^+ \approx k_i^+ / k_{\perp i}^2$, are still ordered as in Eq. (3.126) and as shown in Fig. 3.20. Thus, in terms of time-ordering, the BFKL cascade is quite similar to the DGLAP cascade.

During the long time of parton-cascade evolution a large number of “wee” partons (gluons) are created in the proton’s wave function, as in Fig. 3.20, of order $(1/x)^{\alpha_p-1}$ for BFKL evolution. Each gluon in the cascade is emitted from a pre-existing (larger- x) gluon in the proton’s wave function. Each such “wee” parton interacts with the virtual photon over a very short time. This interaction destroys the coherence of the partons (which are mostly gluons at low x). The further fate of the partons is not important to us since any possible interaction in the final state will not change the total cross section of the deep inelastic

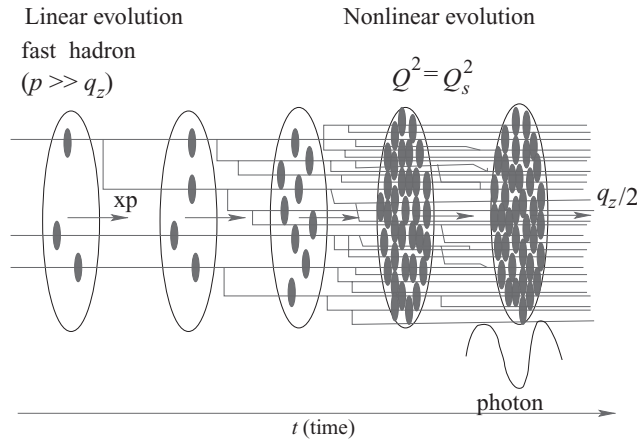


Fig. 3.21. Parton cascade in the Breit frame for DIS (see Sec. 2.3 for the definition of this frame). Both quarks and gluons are denoted by straight lines for simplicity. At the end of the cascade, just before interaction with a virtual photon of wavelength $1/q_z$, the quarks have momentum $q_z/2$ along the collision axis. A color version of this figure is available online at www.cambridge.org/9780521112574.

process. A space–time picture of the QCD evolution that we have just outlined is given in Fig. 3.21; here the straight lines denote both quarks and gluons. The QCD evolution (both DGLAP and BFKL) leads to an increase in the number of “wee” partons with energy. This is a very natural result since both the DGLAP and BFKL equations take into account the emission of partons (along with the virtual corrections). Each emission increases the number of partons at lower energy (i.e., at lower x).

The BFKL evolution creates partons of roughly the same transverse size, as indicated in Fig. 3.16 and discussed in Sec. 3.3.4. As we decrease x the parton density grows. However, at some very small (critical) $x = x_{cr}$, where

$$x_{cr} \sim \left(\frac{Q}{\alpha_s^2 \Lambda_{QCD}} \right)^{1/(\alpha_p - 1)}, \tag{3.127}$$

corresponding to $Q_s(x_{cr}) = Q$, the density of partons in the transverse plane becomes so large that the wave functions of the partons start to overlap, as shown in Fig. 3.21. For such a densely populated system we need to take into account interactions between the partons (Gribov, Levin, and Ryskin 1983).

We conclude that for $Q^2 < Q_s^2$ we should write down a new evolution equation that includes interactions between the partons. This new evolution should slow down and finally stop (*saturate*) the increase in the number of “wee” partons, leading to the saturation of the parton density (Gribov, Levin, and Ryskin 1983). We want to stress again that, since $Q_s^2 \gg \Lambda_{QCD}^2$, the value of the QCD coupling is small and therefore we can apply perturbative QCD methods in the region where unitarity corrections become important.

Our discussion of parton densities is summarized in Fig. 3.22, in our first attempt at constructing a map of high-energy QCD. Figure 3.22 displays the distributions of partons

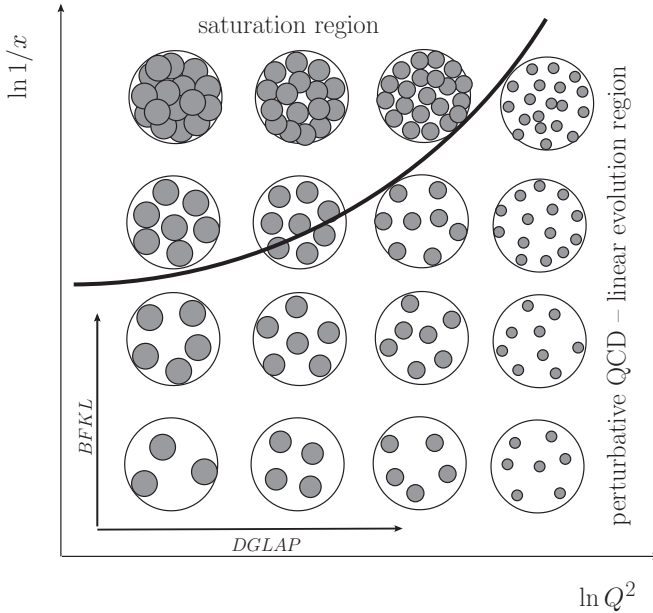


Fig. 3.22. The parton distribution in the transverse plane as a function of $\ln 1/x$ and $\ln Q^2$. The bold curve gives the saturation scale $Q_s(x)$.

in the proton’s transverse plane as a function of Q^2 and x , with the saturation scale (3.125) shown by the bold curve. One can see that this saturation momentum curve divides the entire kinematic region in two parts: the region of perturbative QCD with linear evolution for the parton densities (DGLAP, BFKL) and the saturation domain, in which the parton density is large but the running QCD coupling is still small ($\alpha_s(Q_s^2) \ll 1$). Therefore we need to develop a theoretical description for a system of partons that interact with each other weakly but whose number is so large that we cannot apply the regular methods of perturbative QCD with linear evolution for the parton densities to describe them.

3.4.2 The GLR–MQ equation

To tackle the BFKL unitarity problem and to understand how the growth of the gluon distribution can be tamed, Gribov, Levin, and Ryskin (1983) (GLR) considered the gluon distribution functions of a “dense” proton or a nucleus. By a “dense” proton we mean a proton filled with various sources of color charge (sea quarks and gluons) that were pre-created in the proton’s wave function by some nonperturbative mechanism. Gribov, Levin, and Ryskin argued that for such systems multiple BFKL ladder exchanges may become important; indeed, as we saw in Eq. (3.124), the BFKL equation violates unitarity when the cross section per unit impact parameter, $d\sigma/d^2b$, becomes of order 1. Hence the contribution of double BFKL ladder exchange at this point should be comparable with that of single BFKL ladder exchange. Moreover, owing to the high density of partons, ladder mergers should also be possible as they evolve away from the proton or nucleus in rapidity.

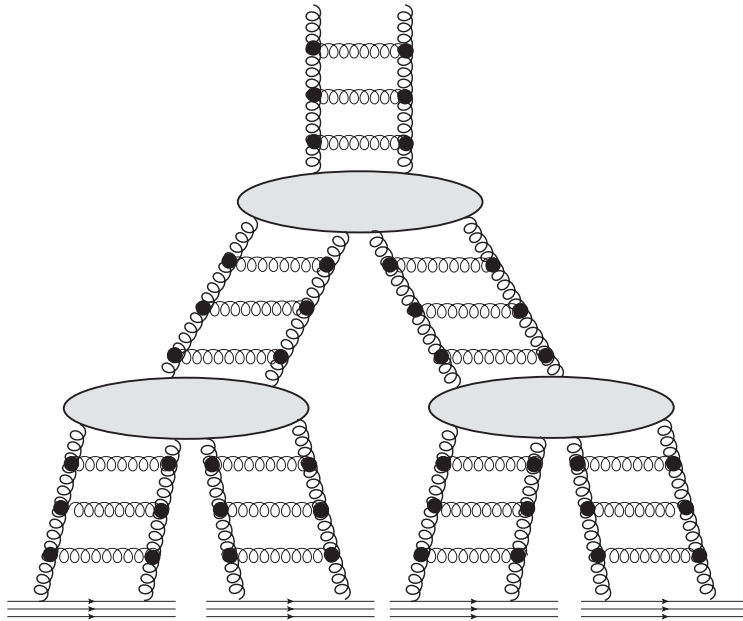


Fig. 3.23. An example of a “fan” diagram resummed by the GLR–MQ equation.

Owing to the large number of partons in the proton or nucleus, the ladders can all connect to different sources of color charge and interact with the proton or nucleus independently. (It may be instructive to mention that in the case of a nuclear target this assumption can be proven to be correct (Schwimmer 1975, Kovchegov 1999, 2000) since the nucleus has a parameter, the atomic number A , allowing one to justify the independent-interaction approximation.) Since we are interested in the gluon distribution, which is a correlation function for two gluon fields, these multiple ladders should all merge in the end into a single ladder, leading to the so-called “fan” diagrams. An example of a fan diagram is shown in Fig. 3.23. There, multiple BFKL ladders start from different quarks and gluons in the proton or nucleus; these are shown by straight lines at the bottom of Fig. 3.23. Owing to the high density of the gluon fields, the ladders cannot stay independent for long. As the energy increases so does the gluon density, eventually leading to *merging* of the ladders, as shown in Fig. 3.23.

Indeed, BFKL ladders can also first split and then recombine, leading to the so-called *pomeron loop* diagrams, one of which is shown in Fig. 3.24. In a purely perturbative picture of the process, such corrections are not enhanced by large parton densities in the proton or nucleus and are therefore subleading. In the original GLR work it was argued that, since the amplitude of a pomeron loop increases with the rapidity interval covered by the loop, the dominant contribution of the pomeron loop diagram as pictured in Fig. 3.24 comes from a loop covering the whole interval in rapidity. It was then argued that in such a contribution the pomeron recombination vertex would be close to the proton in rapidity and, if the proton is nonperturbatively strongly coupled, the vertex can then be effectively absorbed into the

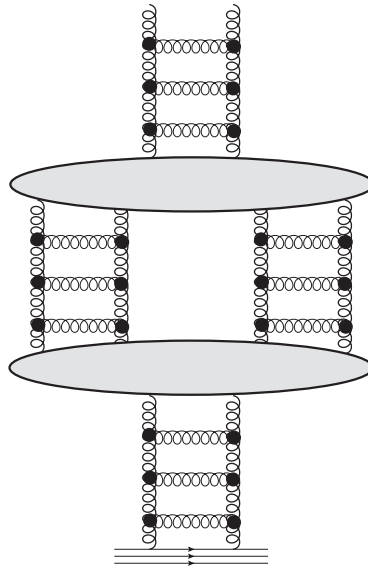


Fig. 3.24. A pomeron loop diagram.

proton. This would make the resulting diagram into a pomeron “fan” diagram, with some complicated nonperturbative interaction with the proton. The latter interaction would then be modeled by independent scatterings of pomeron ladders on different constituents in the proton. We will present the physical parameters justifying the fan diagram approximation in a more systematic way in the next chapter.

Ladder recombination in fan diagrams is described by effective ladder merger vertices, denoted by the ovals in Fig. 3.23. These vertices are called *triple pomeron vertices*, since they connect three different ladders (BFKL pomerons). For their calculation we refer the reader to Bartels and Wusthoff (1995) and Bartels and Kutak (2008) and references therein. If one views the DIS process in the infinite momentum frame described above, the ladder mergers appear to be exactly the partonic interactions that enter when the gluon density becomes high. It turns out that such interactions are not simple individual parton mergers but are, in fact, of a more collective nature, as they consist of ladder mergers, i.e., mergers of different linear parton evolutions.

Note that the diagram in Fig. 3.23 contains only triple pomeron vertices, i.e., $2 \rightarrow 1$ ladder mergers. In the next chapter we will argue that while all higher-order ($3 \rightarrow 1$, $4 \rightarrow 1$, etc.) mergers exist, in the LLA they are suppressed by powers of N_c^2 and can therefore be neglected in the large- N_c (fixed- α_s , N_c) limit (Bartels and Wusthoff 1995, Braun 2000a). Before those results became known, in their original work Gribov, Levin, and Ryskin (1983) had suggested that, before the energy becomes sufficiently high for all nonlinear effects to become important, there could be an intermediate energy region where the physics of gluon distributions is dominated by $2 \rightarrow 1$ ladder recombination. This recombination would bring in a quadratic correction to the linear BFKL equation for the unintegrated gluon distribution

(3.94), leading to the GLR evolution equation (Gribov, Levin, and Ryskin 1983)

$$\frac{\partial \phi(x, k_{\perp}^2)}{\partial \ln(1/x)} = \frac{\alpha_s N_c}{\pi} \int d^2 l_{\perp} K_{BFKL}(k, l) \phi(x, k_{\perp}^2) - \frac{\alpha_s^2 N_c \pi}{2C_F S_{\perp}} [\phi(x, k_{\perp}^2)]^2, \quad (3.128)$$

with the LO BFKL kernel defined in Eq. (3.62). In writing down Eq. (3.128), for simplicity we have assumed that the proton or nucleus has the shape of a cylinder oriented along the beam axis with cross sectional area $S_{\perp} = \pi R^2$; however, the GLR equation (3.128) can be generalized easily to any shape of proton or nucleus, as the impact parameter (b_{\perp}) integration can be carried out separately for each ladder (Gribov, Levin, and Ryskin 1983). As expected, the linear term in Eq. (3.128) is equivalent to the BFKL equation (3.94), while the quadratic term, responsible for ladder mergers, introduces damping and thus slows down the growth of the gluon distributions with energy. This phenomenon became known as the *saturation* of parton distributions. A more quantitative discussion of the role of the damping term on small- x evolution will be presented in the next chapter.

The GLR equation (3.128) was rederived by Mueller and Qiu (1986) in the double leading-logarithmic approximation (DLA) for the integrated gluon distribution function related to the unintegrated distribution by (cf. Eq. (3.93))

$$xG(x, Q^2) = \int^{Q^2} dk_{\perp}^2 \phi(x, k_{\perp}^2). \quad (3.129)$$

Employing the DLA and analyzing diagrams with two merging DGLAP ladders, Mueller and Qiu arrived at the following evolution equation (again written here for a cylindrical proton or nucleus):

$$\frac{\partial^2 xG(x, Q^2)}{\partial \ln(1/x) \partial \ln(Q^2/\Lambda^2)} = \frac{\alpha_s N_c}{\pi} xG(x, Q^2) - \frac{\alpha_s^2 N_c \pi}{2C_F S_{\perp}} \frac{1}{Q^2} [xG(x, Q^2)]^2, \quad (3.130)$$

which is known as the GLR–MQ equation.

Equation (3.130) is easily rewritten in terms of the density of gluons (with transverse size $1/Q$) in the transverse plane,

$$\rho_{glue}(x, Q^2) = \frac{xG(x, Q^2)}{S_{\perp}}; \quad (3.131)$$

we obtain

$$\frac{\partial^2 \rho_{glue}}{\partial \ln(1/x) \partial \ln(Q^2/\Lambda^2)} = \frac{\alpha_s N_c}{\pi} \rho_{glue} - \frac{\alpha_s^2 N_c \pi}{2C_F Q^2} \rho_{glue}^2. \quad (3.132)$$

This equation has a simple probabilistic interpretation, given in Fig. 3.25. There we show several BFKL gluon cascades in the amplitude, each the same as in Fig. 3.20 but drawn in a time-ordered way (cf. Fig. 2.25) in the IMF/Bjorken or Breit frames. The proton or nucleus is envisioned as being at the top of each diagram though not shown explicitly. The first term on the right of Eq. (3.132) clearly describes the emission of an extra gluon at rapidity $Y = \ln 1/x$ (see the left-hand panel in Fig. 3.25), which leads to an increase in

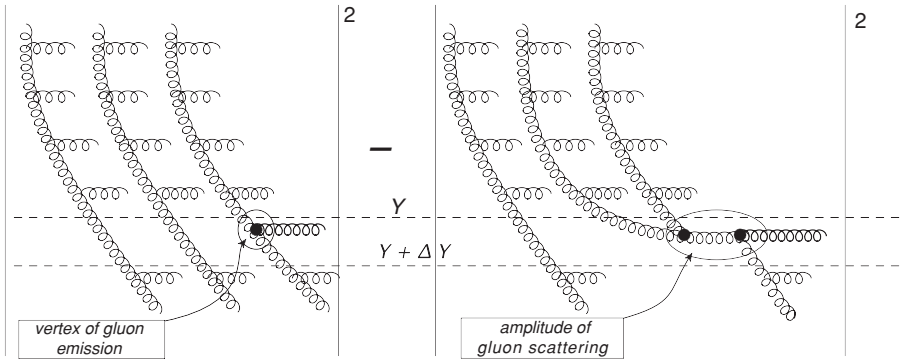


Fig. 3.25. Probabilistic interpretation of the two terms on the right-hand side of the GLR–MQ equation (3.130). The horizontal dashed lines denote one step ΔY of the evolution in rapidity.

the number of s -channel gluons. The gluon can be emitted from any of the three cascades in this panel.

The second term on the right-hand side of Eq. (3.132) corresponds to a process in which two gluon cascades merge together, reducing the number of cascades to two, as shown in the right-hand panel of Fig. 3.25. The s -channel gluon emitted after the merger can only be produced by the two remaining cascades. Thus the cascade merger leads to a decrease in the rate of new gluon production; therefore, it should enter Eq. (3.132) with a minus sign. Since in this process two (t -channel) gluons meet to interact, its contribution is proportional to ρ_{glue}^2 and to the cross section of the $GG \rightarrow GG$ process (see the right-hand panel in Fig. 3.25), which, on dimensional and power-counting grounds, should be proportional to $\sigma \sim \alpha_s^2/Q^2$. This is exactly what goes into the second term on the right-hand side of Eq. (3.132). In the next chapter we will put this probabilistic interpretation on a more rigorous basis.

Equation (3.130) allows one to estimate more precisely the saturation scale Q_s^2 at which the nonlinear saturation effects become important. To do that we have to equate the linear and quadratic terms on the right-hand side of Eq. (3.130). This gives

$$Q_s^2 = \frac{\alpha_s \pi^2}{S_{\perp} 2C_F} xG(x, Q_s^2). \tag{3.133}$$

The gluon distribution near the saturation region grows as a power of $1/x$ at small x (see (3.97)):

$$xG \sim \left(\frac{1}{x}\right)^\lambda, \tag{3.134}$$

with $\lambda > 0$ to be specified in the next chapter in a more detailed estimate. (This behavior of the gluon distribution is supported by experimental data.) Note that for a nucleus consisting of A nucleons we have to multiply this distribution function by the factor A . Using

Eq. (3.134), multiplied by A , in Eq. (3.133) yields

$$Q_s^2 \sim \frac{A}{S_\perp} \left(\frac{1}{x}\right)^\lambda \sim A^{1/3} \left(\frac{1}{x}\right)^\lambda, \tag{3.135}$$

in qualitative agreement with Eq. (3.125). An important additional feature of Eq. (3.135) is that it contains a power of the atomic number A . (In deriving the rightmost expression in Eq. (3.135) we have used the fact that for a nucleus $S_\perp \sim R^2 \sim A^{2/3}$, since $R \sim A^{1/3}$.) This factor $A^{1/3}$ is important: it means that the saturation scale not only grows with decreasing x (increasing energy) but also that it is large for large nuclei. Since nonlinear saturation effects are important for all $Q \lesssim Q_s$, we observe that the saturation region is actually broader for DIS on a nucleus. Also, for the same value of Bjorken x the saturation scale for DIS on a nucleus is larger than that for DIS on a proton, providing a stronger justification for the use of perturbative QCD approach in the former case.

It is instructive to rewrite the saturation condition (3.133) in terms of the transverse gluon density defined in Eq. (3.131). The condition (3.133) implies that

$$\frac{1}{Q_s^2} \rho_{glue}(x, Q_s^2) \sim \frac{1}{\alpha_s}, \tag{3.136}$$

i.e., that the number of gluons in an element of the transverse area comparable with the typical size of the gluon (which is the number of gluons on top of each other in the transverse plane) needs to be of order $1/\alpha_s$ for nonlinear effects to become important. Remembering that $xG \sim \langle A_\mu A_\mu \rangle$, we see from Eq. (3.136) that this implies that the corresponding gluon field should be

$$A_\mu \sim \frac{1}{g}. \tag{3.137}$$

At small coupling this is the strongest that a gluon field can be: the regime of (3.137) sets in when the interaction terms in the QCD Lagrangian (1.1) become parametrically comparable to the kinetic (free) term, as one can see from Eq. (1.4). We have obtained another interpretation of the saturation physics: saturation occurs because the gluon field gets as strong as it can possibly be, leading to the saturation of the gluon field strength and the parton distribution functions. A careful reader might also notice that a strong field of the type (3.137) usually occurs in classical problems, where one is looking for a classical gluon field (e.g. instantons). We will return to this observation and its implications below (McLerran and Venugopalan 1994a, b, c).

When the GLR–MQ equation was originally derived, the quadratic damping term that occurs in both Eqs. (3.128) and (3.130) was believed to be important only near the border of the saturation region, for $Q \sim Q_s$, where nonlinear effects were only starting to become important (Gribov, Levin, and Ryskin 1983, Mueller and Qiu 1986). It was expected that higher-order nonlinear corrections would show up as one goes deeper into the saturation region towards $Q < Q_s$. For instance, a nonlinear AGL evolution equation was proposed by Ayala, Gay Ducati, and Levin (1996, 1997, 1998) that included the suggestion that there should be corrections at all orders in ϕ on the right-hand side of Eq. (3.128). In the next chapter we will present a systematic way of unitarizing the BFKL evolution equation

by including it in the light cone wave function, similarly to how we derived the DGLAP evolution above.

Further reading

For a more detailed and extensive discussion of the pre-QCD pomeron and its phenomenology see Collins (1977), Forshaw and Ross (1997), Barone and Predazzi (2002), and Donnachie, Dosch, and Landshoff (2005).

For readers interested in finding out more details on the BFKL equation and its solution we recommend the article by Del Duca (1995). We also recommend the review of Lipatov (1997), which summarizes everything that was then known about the solution to this linear equation. We believe that any difficulty in reading this paper will be compensated by the beauty of the problem. A very nice and detailed presentation of BFKL physics, gluon reggeization and the bootstrap equation, and higher-order corrections to BFKL evolution can be found in the book by Ioffe, Fadin, and Lipatov (2010).

The triple BFKL pomeron vertex has been extensively studied also. We recommend the paper by Bartels and Kutak (2008) and references therein. One can learn a lot from this paper about the classification and summation of Feynman diagrams in high energy scattering.

Exercises

3.1 Find the quark–quark scattering cross section $d\sigma_{qq \rightarrow qq}/dt$ at the Born level (order α_s^2), expressing the answer in terms of the Mandelstam variables s and t . (For simplicity assume that quarks are massless.) Take the limit of high energy s keeping t fixed and demonstrate that the expression obtained reduces to the cross section found in Sec. 3.2 above. Explain why the diagram in Fig. 3.3 dominates at high energy.

Repeat the above for the Born-level quark–antiquark scattering cross section $d\sigma_{q\bar{q} \rightarrow q\bar{q}}/dt$.

3.2 (a) Derive Eq. (3.24) starting from Eq. (3.18).

(b) Average Eq. (3.24) over the directions of $\vec{x}_{1\perp}$ and $\vec{x}_{2\perp}$ and integrate it over l_\perp to obtain Eq. (3.25).

3.3 Consider onium–onium scattering at fixed impact parameter \vec{b}_\perp .

(a) Generalize Eq. (3.24) to the fixed impact parameter case. You should obtain the following cross section per impact parameter:

$$\begin{aligned} \frac{d\hat{\sigma}_{\text{tot}}^{\text{onium}+\text{onium}}}{d^2b} &= \frac{\alpha_s^2 C_F}{2\pi^2 N_c} \int \frac{d^2l_\perp d^2l'_\perp}{l_\perp^2 l'^2_\perp} \left[e^{i\vec{l}_\perp \cdot (\vec{b}_\perp + \vec{x}_{1\perp}/2)} - e^{i\vec{l}_\perp \cdot (\vec{b}_\perp - \vec{x}_{1\perp}/2)} \right] \\ &\times \left[e^{-i\vec{l}'_\perp \cdot \vec{x}_{2\perp}/2} - e^{i\vec{l}'_\perp \cdot \vec{x}_{2\perp}/2} \right] \left[e^{-i\vec{l}'_\perp \cdot (\vec{b}_\perp + \vec{x}_{1\perp}/2)} - e^{-i\vec{l}'_\perp \cdot (\vec{b}_\perp - \vec{x}_{1\perp}/2)} \right] \\ &\times \left[e^{i\vec{l}_\perp \cdot \vec{x}_{2\perp}/2} - e^{-i\vec{l}_\perp \cdot \vec{x}_{2\perp}/2} \right]. \end{aligned} \tag{3.138}$$

Make sure that integrating Eq. (3.138) over the impact parameter reduces it back to Eq. (3.24).

(b) With the help of Eq. (A.9) integrate Eq. (3.138) over \vec{l}_\perp and \vec{l}'_\perp to obtain

$$\frac{d\hat{\sigma}_{tot}^{onium+onium}}{d^2b} = \frac{2\alpha_s^2 C_F}{N_c} \ln^2 \frac{\left| \vec{b}_\perp + \frac{1}{2}\vec{x}_{1\perp} + \frac{1}{2}\vec{x}_{2\perp} \right| \left| \vec{b}_\perp - \frac{1}{2}\vec{x}_{1\perp} - \frac{1}{2}\vec{x}_{2\perp} \right|}{\left| \vec{b}_\perp + \frac{1}{2}\vec{x}_{1\perp} - \frac{1}{2}\vec{x}_{2\perp} \right| \left| \vec{b}_\perp - \frac{1}{2}\vec{x}_{1\perp} + \frac{1}{2}\vec{x}_{2\perp} \right|}. \tag{3.139}$$

3.4 Show that the azimuthally symmetric eigenfunction $\chi(0, \nu)$ of the BFKL kernel from Eq. (3.81) reduces to

$$\chi(0, \nu) = \frac{4}{1 + 4\nu^2} \tag{3.140}$$

if we extract only the leading twist contributions to the BFKL Green function in Eq. (3.82) for both $l_\perp \gg l'_\perp$ and $l_\perp \ll l'_\perp$.

3.5 Use Eq. (3.82) in Eq. (3.26) to find the total onium–onium scattering cross section due to a BFKL pomeron exchange (neglecting the light cone wave functions of the onia).

(a) First the integration over l_\perp and l'_\perp . You may find formulas (A.16) and (A.19) handy.

(b) Use the expansion around the saddle point given in (3.84) to perform the remaining ν -integral using the steepest descent method. You should obtain

$$\hat{\sigma}_{tot}^{onium+onium} = \frac{16\alpha_s^2 C_F}{N_c} x_{1\perp} x_{2\perp} \sqrt{\frac{\pi}{14\zeta(3)\bar{\alpha}_s Y}} \times \exp \left\{ (\alpha_P - 1)Y - \frac{\ln^2(x_{1\perp}/x_{2\perp})}{14\zeta(3)\bar{\alpha}_s Y} \right\}. \tag{3.141}$$

3.6 Verify explicitly that the BFKL Green function (3.80) satisfies the property (3.120).